INLET SHAPE CONSIDERATIONS FOR SPLIT-WING ELECTRIC DISTRIBUTRED PROPULSION

A Thesis

presented to

the Faculty of California Polytechnic State University

San Luis Obispo

In Partial Fulfillment

Of the Requirements of the Degree

Masters of Science in Aerospace Engineering

by

Kurt VonderHaar Papathakis

June 2015

COMMITTEE MEMBERSHIP

TITLE:	Inlet Shape Considerations for Split-Wing Electric Distributed Propulsion
AUTHOR:	Kurt VonderHaar Papathakis
DATE SUBMITTED:	June 2015
COMMITTEE CHAIR:	Dr. David Marshall, Professor, Aerospace Engineering
COMMITTEE MEMBER:	Dr. Robert McDonald, Associate Professor, Aerospace Engineering
COMMITTEE MEMBER:	Dr. Paul Choboter, Professor, Mathematics Department
COMMITTEE MEMBER:	Benjamin Schiltgen, Aerospace Engineer / VP-Finance, Empirical Systems Aerospace, Inc.

ABSTRACT

Inlet Shape Considerations for Split-Wing Electric Distributed Propulsion

Kurt VonderHaar Papathakis

This thesis aims to uncover preliminary design relationships for an inlet of a split-wing electric distributed propulsion regional airliner. Several aspects of the inlet design were investigated, including: the overall thickness of the airfoil section with respect to the chord, inlet throat area, and lip radius. These parameters were investigated using several angles of attack and mass flow rates through the fan. Computational fluid dynamics, with a 2nd Order turbulence model was used and validated against World War II era data from NACA, as those studies were the most pertinent wind tunnel data available. Additionally, other works by Boeing, Empirical Systems Aerospace (ESAero), Rolling Hills Research, and the Air Force Research Laboratories (AFRL) were considered as part of this design tool tradespace. Future work considerations include utilizing an airfoil section designed for M = 0.6 or 0.65 cruise conditions as opposed to a symmetrical airfoil section, extruding the 2-D airfoil section discussed in this thesis for 3-D effects, and incorporating fan rotational physics into the simulations to better account for inlet Mach number effects.

Keywords: Split-Wing, Electric Propulsion, Hybrid-Electric Propulsion, Inlet Design, Distributed Propulsion, CFD, N+3 Aircraft Design

ACKNOWLEDGMENTS

I would like to acknowledge the following people who have made this thesis possible. Firstly, to my fiancée / wife Lindsay for supporting me through the moves, new jobs, wedding, pregnancy, baby, and all the ups and downs of the past few years. Without her, this thesis would never have been completed. Secondly, I would like to acknowledge Andy, Ben, Trevor, and the rest of ESAero who gave me an opportunity to study in this field and an ability to work with them and complete my studies. Lastly, I would like to acknowledge my co-workers at NASA Armstrong who have given me aid and encouragement since I began working there in 2013.

TABLE OF CONTENTS

LIST OF TABLES

LIST OF FIGURES

NOMENCLATURE

$A_{capture}$	Capture Area
A_{th}	Throat area
$\bar{A}_{th}$	Throat area ratio
A_2	Fan face flow area
$\propto$	Angle-of-Attack
ARMD	(NASA) Aeronautics Research Mission Directorate
BMS	Battery Management System
BWB	Blended Wing Body
c	chord
C_D	Coefficient of Drag
C_L	Coefficient of Lift
C_{L_max}	Coefficient of Lift, maximum
c_l	Sectional Coefficient of Lift
C_P	Coefficient of Pressure
CFD	Computational Fluid Dynamics
$(\delta^*/r)_{th}$	Boundary Layer at the throat
DEP	Distributed Electric Propulsion
EMI	Electro-Magnetic Interference
ε	Discretized error
$\tilde{f}$	Exact solution to original partial differential equations
f_h	Exact solution to discrete equation
FPR	Fan Pressure Ratio
γ-Re_θ	Transition model
HEIST	Hybrid-Electric Integrated Static Testbed

HWB	Hybrid Wing Body
k-ω	Turbulence Model (2 equation)
K_D	Empirical Diffuser Total Pressure Loss Factor
K_{Mth}	Empirical Throat Mach Number Factor
LEAPTech	Leading Edge Asynchronous Propeller Technology
LRR	Lip Radius Ratio
M	Mach Number
M_0	Freestream Mach Number
M_{th} or M_1	Throat Mach Number
$\dot{m}$	Mass Flow Rate
(m/m*)	Mass Flow Rate Ratio
mot	Electric Motor Diameter (in)
N+3	Third Generation (2025-2030)
NACA	National Advisory Committee for Aeronautics
NARI	NASA Aeronautics Research Institute
NASA	National Aeronautics and Space Administration
OEI	One Engine Inoperable
OFI	One Fan Inoperable
p	Local Static Pressure
$\frac{P_2}{P_{th}}$	Diffuser Pressure Ratio
p_{th}/P_{th}	Ratio of Static to Total Pressure
q	Free-stream Dynamic Pressure (½ρv^2)
Re	Reynolds's Number
ρ	Density
SBIR	Small Business Initiative Research
SST	Turbulence Model with Eddy-Viscosity (2 equation)

STOL	Short Takeoff and Landing
τ	Torque
TeDP	Turbo-electric Distributed Propulsion
toc	Total Airfoil Thickness Over Chord (%)
TOGW	Takeoff Gross Weight
TRL	Technology Readiness Level
V	Free-stream Velocity
VTOL	Vertical Takeoff and Landing
WOT	Wide Open Throttle
y+	Boundary Layer Thickness

1. Introduction

1.1 Motivation – N+3 Transformative Change for Regional Airliners

The motivation for this thesis stems from the 2012 NASA N+3 performance goals for 2025 regional airliners identified in the NASA N+3 guidelines [8] shown below:

Table 1: NASA N+1, N+2, and N+3 guidelines for regional airliner improvements in noise, NOx emissions, fuel burn, and field length. [1]

TECHNOLOGY BENEFITS*	TECHNOLOGY GENERATIONS (Technology Readiness Level = 4-6)		
	N+1 (2015)	N+2 (2020**)	N+3 (2025)
Noise (cum margin rel. to Stage 4)	-32 dB	-42 dB	-71 dB
LTO NOx Emissions (rel. to CAEP 6)	-60%	-75%	-80%
Cruise NOx Emissions (rel. to 2005 best in class)	-55%	-70%	-80%
Aircraft Fuel/Energy Consumption‡ (rel. to 2005 best in class)	-33%	-50%	-60%

There were four primary performance metrics identified as part of this technology roadmap: noise reduction, reduction in emissions at the airport (LTO NOx Emissions), reduction in emissions at altitude (Cruise NOx Emissions), and reduction in fuel / energy consumptions. These goals guide the research and development paths for the green aviation initiative under the Aerodynamics Research Mission Directorate (ARMD) of NASA. This thesis presents a specific configuration that has been initially demonstrated in a Small Business Initiative Research (SBIR) project to effectively or partially meet this aggressive technological milestones: the split-wing electric distributed propulsion regional airliner. The split-wing configuration leverages an electric distributed propulsion system to improve upon the abovementioned performance metrics.

1.2 Benefits and Drawbacks of Electric Distributed Propulsion

Electric distributed propulsion is a method of delivering power to various propulsive devices, and in the case of this study, to electric motors powering ducted fans. Instead of creating and using power from the fuel at a single location (i.e. current jet engines pod-and-wing configurations), electric distributed propulsion grants significant flexibility to the design of the propulsion system and overall aircraft design by allowing the gas generator and propulsors to be separated and placed in various, and aerodynamically beneficial locations. With vast improvements in battery and electric motor technologies, electric distributed propulsion can now be used to maximize fuel economy and provide unique design opportunities such as yaw control, powered lift, wing-tip thrust, and windmill charging.

Electric distributed propulsion system architectures typically include: thrust generators (rotors / fans / propellers), electric motors and generators, electronic speed controllers, electricity conversion components (converters / inverters / rectifiers / transformers), power cables, batteries and battery management systems (BMS), electrical buses, engines, and thermal management systems. There are several types of electric and hybrid-electric architectures available, including: all-electric (battery or supercapacitor powered), turbo-electric (turbine generator), parallel hybrid (multi-drive), series hybrid (single-drive), and distributed propulsion (generator(s) separated from thrust device(s)). The focus of this thesis is electric (or hybrid-electric) distributed propulsion, so no parallel hybrid systems are considered.

Electric distributed propulsion represents one possible path for meeting the noise, emissions, and fuel/energy consumption goals, shown in Table 1. NASA has identified eight methodologies for addressing the N+3 goals: Tailored Fuselages, High AR Elastic Wings, Quiet Simplified High-Lift Devices, High Efficiency Small Gas Generators, Hybrid Electric Propulsion, Propulsion Airframe Integration, Tools, and Alternative Fuels[(1)]. Electric and hybrid-electric distributed propulsion satisfies two of those methodologies: hybrid electric propulsion and propulsion airframe integration. Both methodologies aim to reduce fuel/energy consumption, reduce NOx emissions, and reduce noise.

"Electric propulsion is a scale-independent technology encouraging distribution due to compactness, power/weight, efficiency, and motor heat rejection. This is not true for existing reciprocating and turbine propulsion solutions."[26]

There are several benefits to the electric (or hybrid-electric) distributed propulsion system. Distributing thrust enables designers to place thrust producers (i.e. turbofans, ducted fans, propellers, etc.) at high drag locations, particularly at the wingtips. Wingtip propulsors were investigated in the 1970's and '80's as a method for countering the adverse wingtip vortices, with significant drag reduction capabilities. However, there was no practical application as the weight of the turbine engines (turbojet engines) and fuel lines were so significant that the wing structure necessary to support this configuration precluded any future investigation. Distributed propulsion represents one of the first enabling technologies for wingtip propulsors, as the propulsors themselves (motor / fan assemblies) are relatively light, which makes the structural implications feasible.

Energy efficiency / fuel burn savings is achieved by allowing designers to size the engines (e.g. turbogenerators) for cruise performance instead of takeoff or top-of-climb requirements. Currently, these high thrust conditions necessitate the overall design of the engines to be increased, pushing them away from cruise efficiency point. Electric (or hybrid-electric) distributed propulsion provides designers more flexibility in the designs, as battery power can be used to augment in high thrust conditions. This principle can also be applied to new wing designs, utilizing powered lift to allow designers the ability to size the wing for cruise efficiency and drag reduction.

Another benefit to electric distributed propulsion is noise reduction. By reducing the size of the fans / propellers, the overall noise generated by the system dramatically decreases. Distributing the propulsion to numerous, smaller propulsors allows designers to maintain thrust requirements while reducing the size of the fans / propellers.

The current drawbacks for electric and hybrid-electric propulsion are cruise speed and system complexity. Electric (and potentially hybrid-electric) solutions cannot feasibly maintain high cruise speeds for long ranges. Transformative change won't occur until speeds of M = 0.65 and

greater can be achieved. Even at those reduced speeds (from conventional B737), shorter ranges will be necessary until the battery technology broadens the currently narrow electric (or hybrid-electric) flight envelope. The good news is that each technology jump opens up a new portion of the electric and hybrid-electric envelopes.

System complexity concerns usually accompany radical design architecture changes and are expected. These inherit complexities will retard the integration and manifestation of these technologies due to safety, airworthiness, and redundancy concerns.

NASA has developed a spiral development program for improving electric and hybrid-electric technology readiness level (TRL), see Figure 1 and Figure 3.

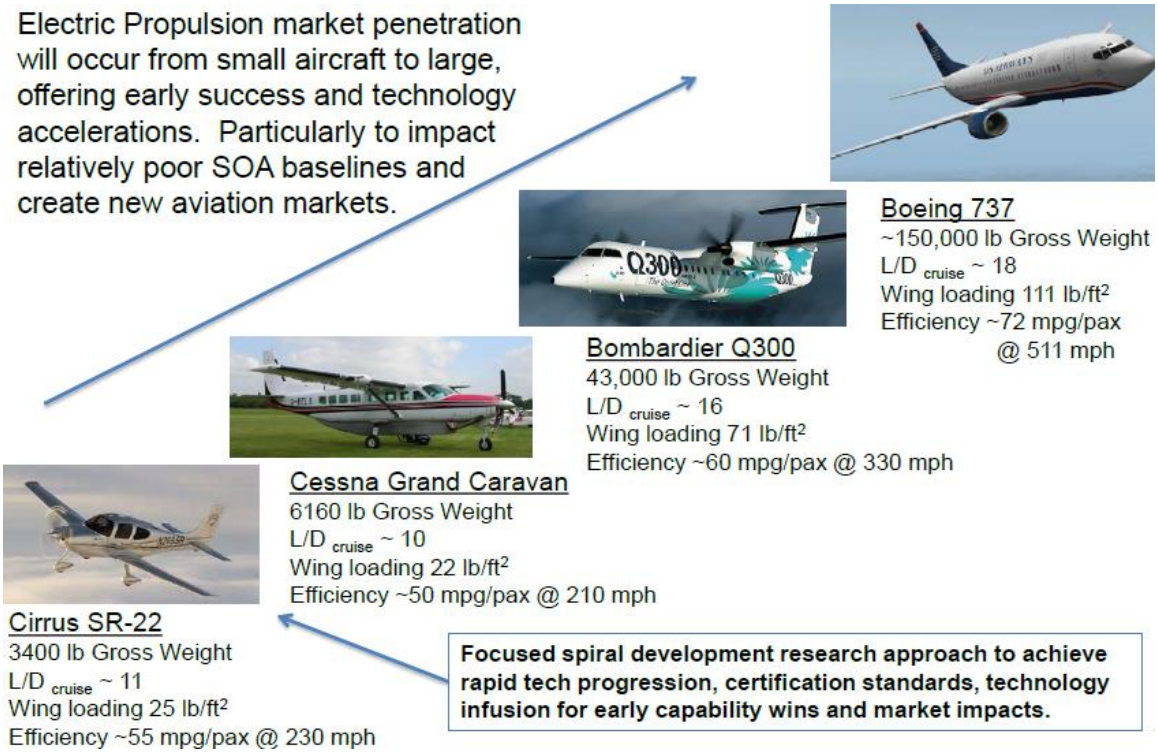

Figure 1: NASA LEAPTech Distributed Electric Propulsion roadmap © 2012.[27]

As part of the effort to push electric and hybrid-electric innovation, NASA is currently working on a project named Leading Edge Asynchronous Propeller Technology (LEAPTech) that is delving into both the electric distributed propulsion and propulsion airframe integration. See Figure 2. This project represents a risk-reduction exercise designed to answer flight safety concerns before a light, general aviation, electric distributed propulsion aircraft is pursued.

"All research will provide significant value and risk reduction as this research transitions to larger, flight demonstrations."[26]

Figure 2: LEAPTech truck rig concept and initial low-speed testing © 2015.[4,25]

In order for the aircraft systems design to keep up with the technology jumps, electric and hybrid-electric architectures must be developed concurrently with the development of new battery / supercapacitor technologies. The starting point is risk reduction for a light, general aviation, internal combustion engine airplane and methodically move toward larger and more complex systems until the technologies, budgets, and expertise are available for the B737 replacement.

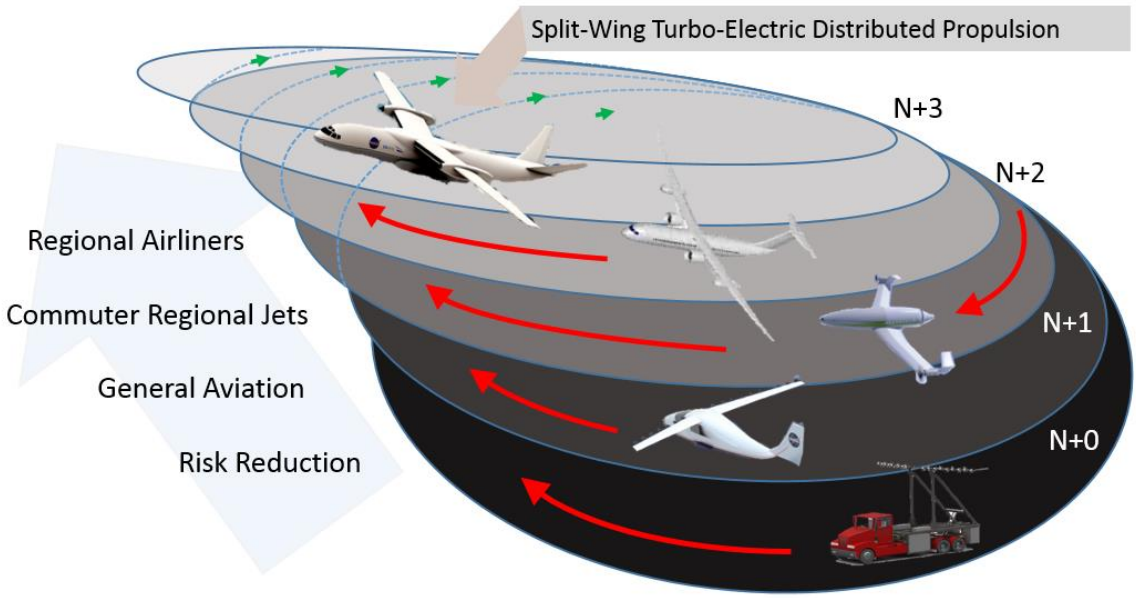

Figure 3: Split-wing turbo-electric distributed propulsion spiral development strategy.

Figure 3 shows a spiral development process culminating in the B737 replacement goal (denoted as a split-wing turbo-electric distributed propulsion regional airliner). The LEAPTech truck and wing experiment provides risk reduction to help develop the necessary technology and integration strategies required for an electric general aviation airplane. Each path around the spiral systematically increases the complexity and capability of the technology. The N+2 spiral represents the commuter regional jets or 60 passenger turboprop electric / hybrid-electric propulsion. The N+2 / N+3 design shown is the Boeing SUGAR aircraft, designed specifically as a regional airliner replacement for both the 737 and 757 lines. The final spiral combines the B737 replacement power architecture of the Boeing SUGAR with the smaller, more efficient ducted fan architecture inherent in the split-wing design.

With a successful risk reduction exercise, the focus shifts to the General Aviation (GA) category. NASA has several goals for this phase of the development, including:

- Efficiency: ~8x reduction in energy use
- Emissions: ~5x reduction in greenhouse gases
- Acoustics: ~30 dB reduction in aircraft noise generation
- Cost: ~12x reduction in energy cost (~4x with battery amortization)
- Field Length / Ride Quality: Increased effective C_{L_max} to achieve wing loading ~2.5x higher at constant field length, or constant wing loading to achieve STOL capability

The next phase would be to design a larger (commuter regional jet category) electric or hybrid-electric aircraft testbed.

> *"Understand how DEP enables new vehicle capabilities through tight coupling of propulsion to the entire vehicle system, with initial focus on the high-lift system, aerodynamics, acoustics, control, structures, and aeroelastics."*[27]

Below in Figure 4 is a capability timeline for NASA in 2012. It depicts goals for 2016, 2019, and 2022 which essentially equate to the General Aviation (GA), Commuter Regional Jets (RJs), and Large Commercial categories shown in Figure 3.

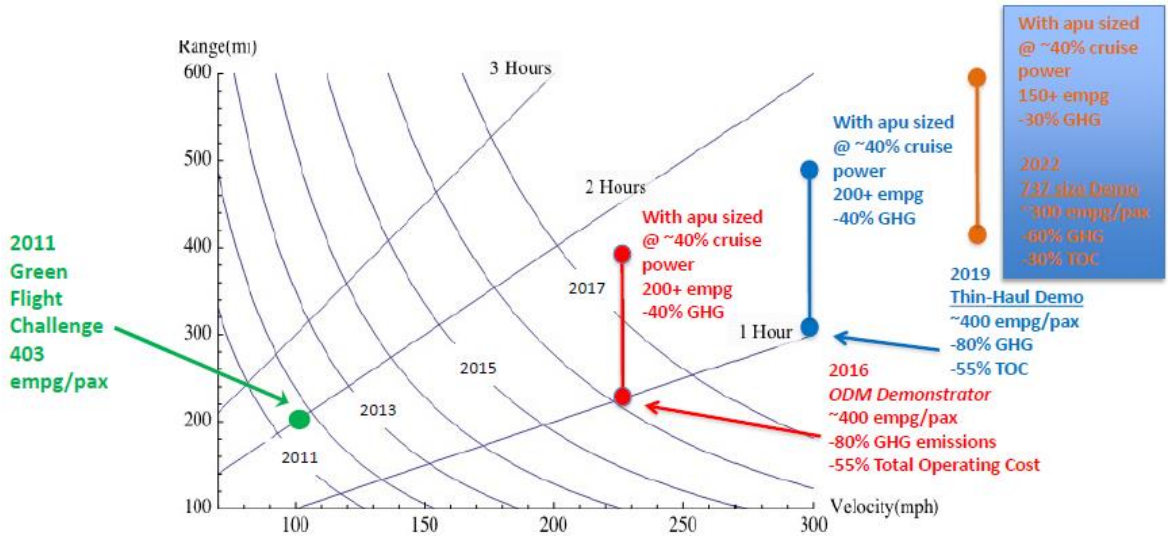

Figure 4: NASA DEP capability timeline © 2012.[35]

Larger, twin-aisle aircraft have also been investigated, but generally for high gross weight, long mission aircraft, electric and hybrid-electric technologies are not currently feasible. In most cases, the added weight of an electric / hybrid-electric propulsion system would prevent the design from even closing. Other distributed propulsion configurations have been investigated, including the blended-wing-body (BWB) and hybrid-wing-body (HWB). However, the BWB and HWB are notoriously un-scalable, and only feasible as a B767 / B777 replacement. The BWB and HWB do not scale to single-aisle and regional jet markets.

> *"Initial NASA Electric Propulsion studies have focused on applications to the long range, high Mach, twin-aisle vehicle class (i.e. N3-X BWB); this is not a good fit for technology infusion."*[26]

While BWB and HWB configurations may present a possible electric / hybrid-electric replacement for long-haul aircraft (i.e. B767, 777, 747, etc.) , the configuration is difficult to spiral develop, as the blended wing body concept gets distorted for small aircraft due to significantly higher drag compared to the single-aisle, tube-and-wing configuration of most commercial aircraft. These configurations would require large-scale demonstrators with significant scope and risk.

Electric and hybrid-electric propulsion provides other avenues for significant improvements to overall flight performance, including noise reduction and reduced field length. Other NASA

projects focus on smaller electric distributed propulsion, investigating how to utilize STOL and VTOL capabilities and with an all-electric distributed propulsion architecture, as seen in Figure 5. Additionally, acoustic testing on propeller phasing on these distributed propulsion systems has also begun.

Figure 5: NASA long endurance VTOL DEP Demonstrator © 2012.[35]

1.3 Configuration Types for Electric Distributed Propulsion

There are numerous configuration types available for electric distributed propulsion, including over-wing, under-wing, split-wing, wingtip, and fuselage pylon configurations. Over-wing configurations place the propulsors over the wing, and typically capitalize on boundary layer ingestion techniques. Under-wing is the current mainstream configuration, with large podded nacelles hanging from the wings. Both the over-wing and under-wing can be both conventional turboprop / turbofan (depending on speed/size/range) or distributed propulsion designs. Fuselage pylon configurations are generally smaller regional aircraft size, due to the noise issues stemming from the close proximity of the jet engines to the passengers. However, with distributed propulsion, this configuration would have significant design flexibility. The split-wing configuration places the propulsors inside the wing, essentially splitting the wing from leading to trailing edge and placing the electric distributed propulsors inside the cavity. The primary drivers for this design are reducing the adverse pressure at the leading edge of the airfoil by making it the inlet to the propulsion system, provide powered-lift, and vectored thrust.

1.4 Split-Wing Concept

There are benefits and drawbacks to each of the configuration types listed above, including specific ramifications for electric and hybrid-electric applications. While the under-wing configuration is the staple and various studies have investigated the over-wing approach, very little research has been completed for the aerodynamic interactions and design criteria for a split-wing configuration. It is currently unknown if the split-wing configuration will be effective or an attractive option compared to over-wing, under-wing, wingtip, fuselage-mounted, or other configuration made available by these hybrid-electric and fully electric technologies. This tool aims to provide some insight into the propulsion-aerodynamic interactions for the split-wing configuration; the specific motivation of this thesis is to provide an initial design trade study and tools for future developers to better understand how the size of the motors, including the diameter and length, the thickness of the airfoils, and other parameters relate to the overall configuration as well as provide parameterized configuration pressure distributions.

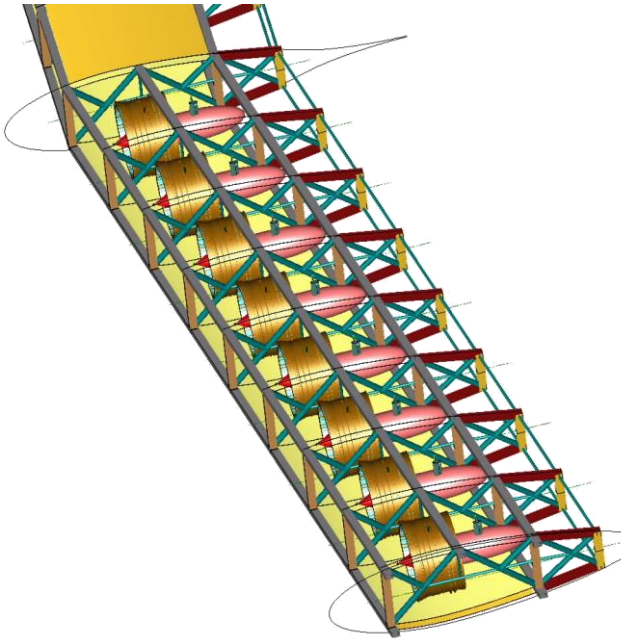

Figure 6: Solid model of an inboard split-wing fan-motor array [13].

This study utilized geometry from a 2-D cross-section of a preliminary design of a turboelectric distributed propulsion (TeDP) Boeing 737 (B737) replacement. Several key dimensions (throat area, wing thickness, inlet shape) and flight conditions (takeoff, top-of-climb, and cruise) were evaluated in this study to identify inlet design relationships for a split-wing configurations.

1.4.1 Benefits

The benefits of the split-wing configuration over the other electric and hybrid-electric configurations are increased flexibility for wing / fan / motor design, reduction in adverse leading edge pressure distributions, thrust vectoring potential, yaw / roll control using the propulsion system, STOL capability, reduced noise, and propulsion system redundancy. While some of these attributes can be applied to the other configurations, the split-wing does present some exciting new design possibilities.

1.4.2 Drawbacks

There are some drawbacks to this design as well, including adverse scavenging of neighboring fans, complicated structural considerations inside the wing, and geometry conversions from rectangular inlets to circular fan cowlings back to rectangular nozzles. Additionally, added scrutiny would accompany this novel design concept, through the design, manufacture, and test sequences.

1.4.3 Unanswered Questions

This thesis aims to provide some insight into shape considerations for the split-wing configuration. It is currently not known how the split-wing configuration will perform during low-speed operations, how the rectangular inlet will drive the design of the propulsion system, how effective the split-wing concept can preserve the inlet pressure ratios for geometric changes, and whether any perceived benefits would amount to a competitive electric or hybrid-electric alternative to over-wing, under-wing, wingtip, or fuselage pylon configurations.

2. Background

2.1 All-Electric and Hybrid-Electric Propulsion for Aircraft

The Boeing SUGAR (Phase II) project represents a significant accomplishment in hybrid-electric regional airliner replacement. The SUGAR project starting in 2009 as the Subsonic Ultra Green Aircraft Research (SUGAR) project tasked with identifying and analyzing advanced concepts and technologies for aircraft in the 2030-2035 timeframe. Boeing decided to go with the truss-braced wing concept, with hybrid-electric propulsion.

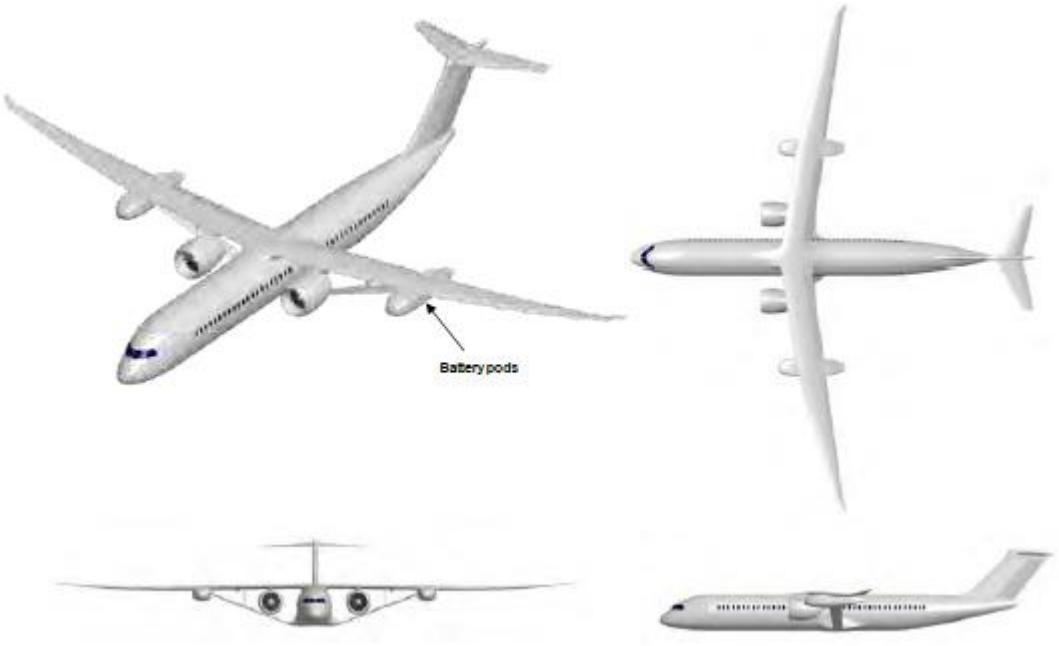

Figure 7: Boeing SUGAR High Voltage Configuration.[5]

The airframer's goals for the SUGAR project were,

- Design and analysis of hybrid-electric gas turbine propulsion
- Comprehensive study of high aspect ratio truss braced wing
- Additional noise technologies
- Synergistic benefits of methane and/or hydrogen fuel

Boeing investigated several design tradespaces and developed their own development strategy for developing a hybrid-electric B737 replacement. See Figure 8. Notice that Boeing is

still considering the BWB with the bottom row. The SUGAR project is planning for an N+3 (i.e. 20-30 years from now) as their target for insertion into market for hybrid-electric.

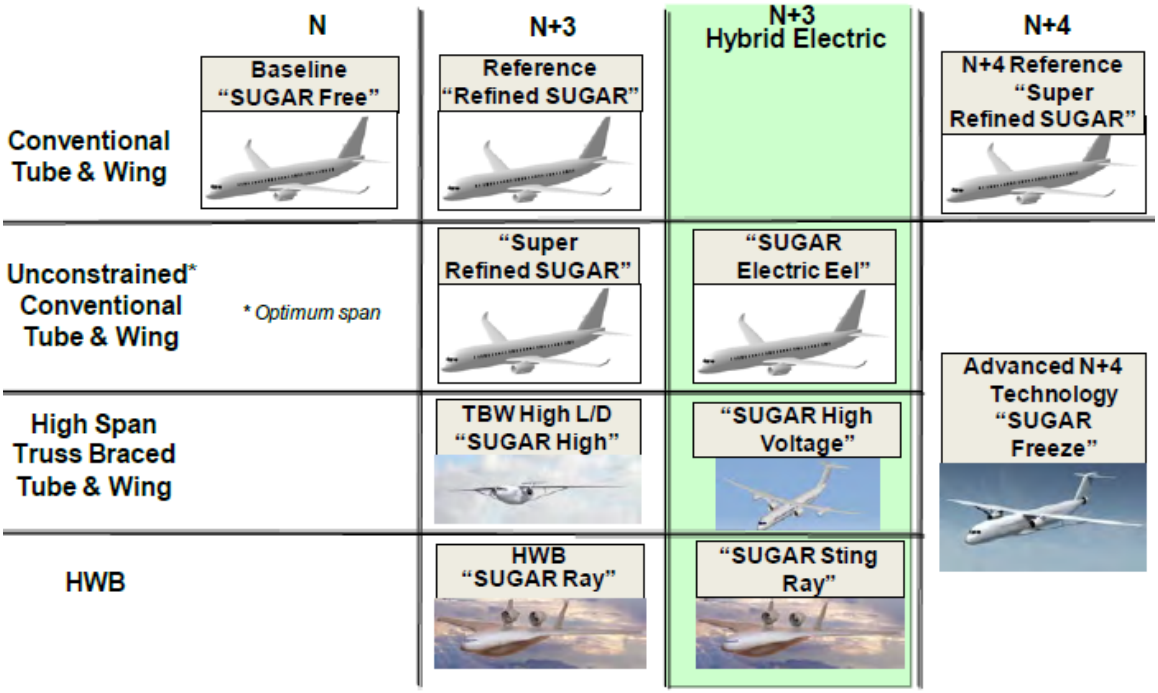

Figure 8: Boeing SUGAR hybrid-electric concepts.[5]

The SUGAR project produced several interesting findings, including estimates on ideal range and electric propulsion sizing guidelines. Figure 9 shows both the effects of hybridizing (adding partial electric propulsion to a jet airliner) and the overall battery weight estimation. Interestingly, the larger 10,000 HP hybrid system offers improved fuel burn for average missions, but actually becomes counterproductive at larger ranges. Also of note, the battery system becomes lighter above 2200 mile range. Unfortunately, that information was not available, but these configurations are inherently non-linear.

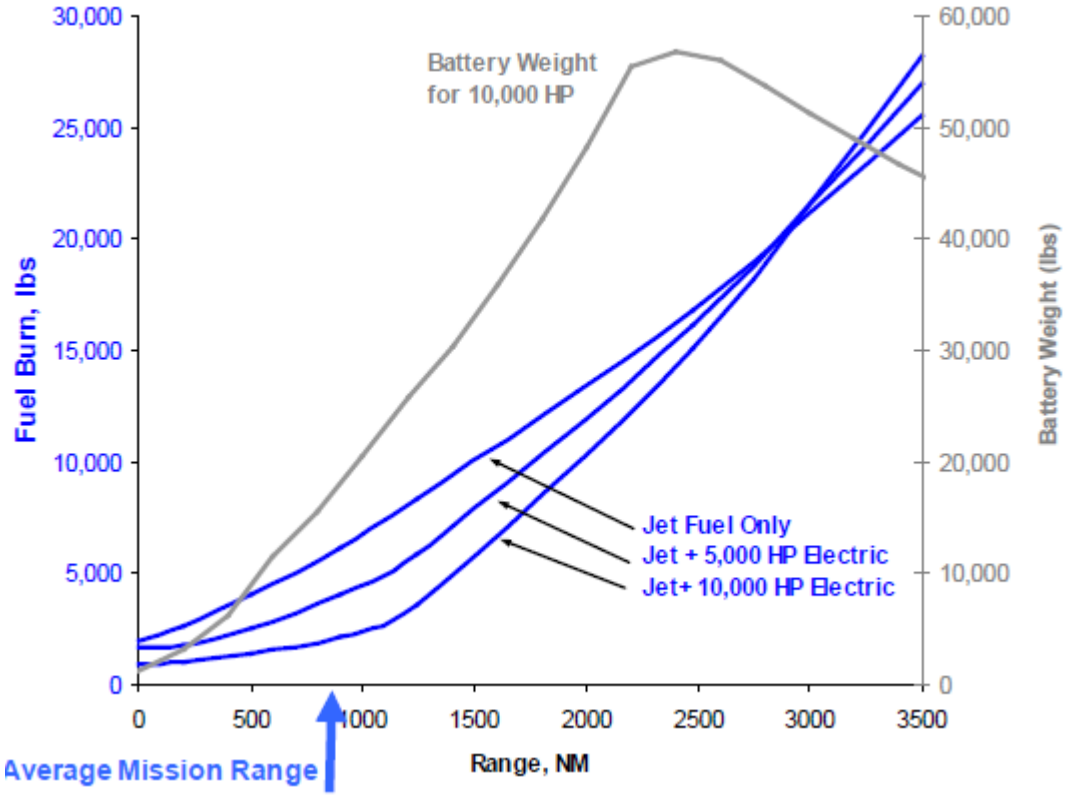

Figure 9: Boeing SUGAR hybrid-electric tube and wing sizing results.[5]

NASA is also working on their electric propulsion spiral development plan. One of the key phases of their plan is the Leading Edge Asynchronous Propeller Technology (LEAPTech) project investigating distributed electric propulsion, using a general aviation demonstrator (phase one from Figure 3.

LEAPTech has numerous project goals, all pertaining to the improvement of the NASA capability roadmap presented in Table 1; ultimately, the goal of the LEAPTech aircraft is to develop an electric distributed propulsion asset that will fulfill both roles of being a risk reduction investigation for phase one of the spiral development plan (Figure 3), and provide a meaningful testbed for electric distributed flight, acoustics, and myriad aerodynamic benefits available due to distributed propulsion.

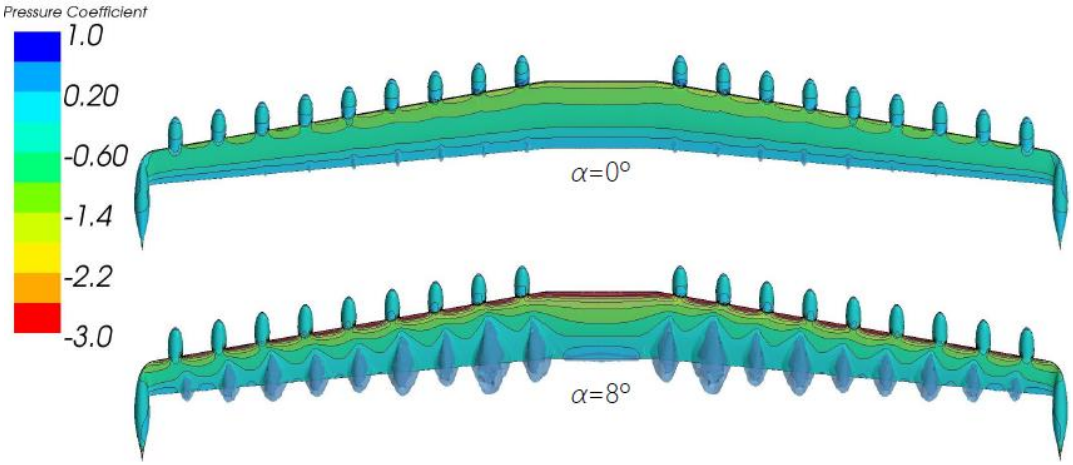

Figure 10: (top) LEAPtech concept rendered in cruise. Majority of leading edge propellers are folded back to minimize drag. (bottom) Initial CFD performed on takeoff for 0º and 8º angle of attack. [35]

The general aviation rendering in Figure 10 shows phase one of the roadmap in Figure 3, utilizing the techniques and results from LEAPTech and other projects and produce a pilotable, electric-distributed propulsion platform. Ideally, this effort would grow into an X-plane type NASA project to further bolster both NASA's core competencies and help small and large national businesses capitalize on the findings. The group consisted of NASA Ames, Armstrong, Glenn, and Langley as well as two small businesses: ESAero and Joby Aviation.

> *"LEAPTech is a key element of NASA's plan to help the aircraft industry transition to electrically propelled planes."*[35]

The project had several unique characteristics, including: foldable propellers, all-electric, distributed propulsion, and cruise-designed wing. Current designs suggest 18 propeller / motor / inverter, 16 identical inboard propulsors and 2 wing-tip propulsors.

The lower CFD results in Figure 10 shows coefficient of pressure (C_P) distributions for angle of attack (α) of 0º and 8º over the cruise wing during takeoff (powered-lift) conditions. The CFD analysis was performed using STAR-CCM+ on an unstructured mesh, using Navier-Stokes theorem with an SST (Menter) k-ω turbulence model and a γ-Re_θ transition model.

Initial testing on LEAPTech has suggested very positive performance benefits going forward with this project and others with regards to the powered lift provided by the electric distributed propulsion.

2.2 Split-Wing Electric Distributed Propulsion Design

Empirical Systems Aerospace, Inc. (ESAero) has developed a split-wing turbo-electric distributed propulsion design presented in both a commercial regional airliner configuration and a dual-use military cargo variant, shown in Figure 11 and Figure 12. Several NASA-funded SBIR efforts as well as privately funded projects have focused on creating hybrid-electric aircraft configurations, hybrid-electric architecture design, performance analyses, and fan design tools focused on incorporating and maturing this split-wing concept [10,11,13,32].

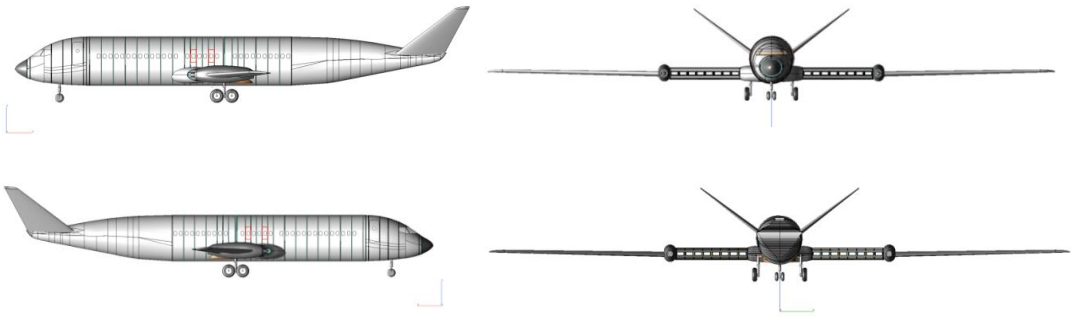

Figure 11: Commercial regional airliner configuration incorporating split-wing turbo-electric distributed propulsion architecture. [10,11]

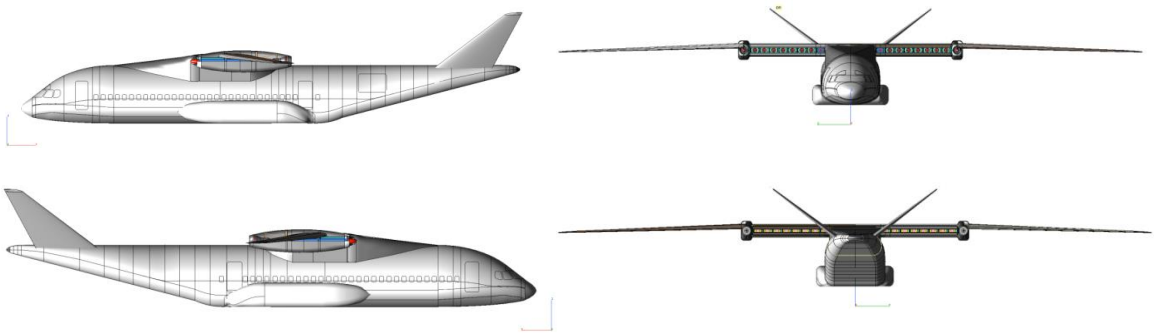

Figure 12: Military cargo configuration incorporating split-wing turbo-electric distributed propulsion architecture. [10,11]

The fan propulsion system was designed using HAPSS, an ESAero fan design tool developed by Michael Green[16]. The code sizes the turbo-generator, electric motors, generators, batteries, as well as designs the fans using 1-D and 2-D methods for on-design and off-design conditions. Table 2 depicts HAPPS outputs used to size a baseline fan / motor assembly for this study.

Table 2: HAPSS hybrid-electric system architecture design for commercial and military cargo split-wing configurations[16].

Parameter	Units	Commercial		Military Cargo	
		Motor	Generator	Motor	Generator
Max Performance					
Power	hp	1267	10684	1843	15539
Speed	RPM	15693	14545	13013	14545
Torque	ft-lb	921	8382	1616	12191
Top-of-Climb Performance					
Power	hp	743	6384	1081	9285
Speed	RPM	9416	8000	7808	8000
Torque	ft-lb	415	4191	727	4191
Takeoff Performance					
Power*	hp	1275	11005	1912	16521
Speed	RPM	8902	8000	7346	8000
Torque	ft-lb	752	7225	1367	7225
Motor / Generator Sizing					

Length	in	59.6	151.5	71.9	151.5
Diameter	in	7.3	13.8	8.8	16.6
Weight	lb	514	2486	678	3279
Controller Weight†	lb	154	746	203	984
Power Density	hp/lb	2.46	4.30	2.72	4.74

The inboard hybrid electric propulsion architecture was built-up using solid modeling, as shown in Figure 13.

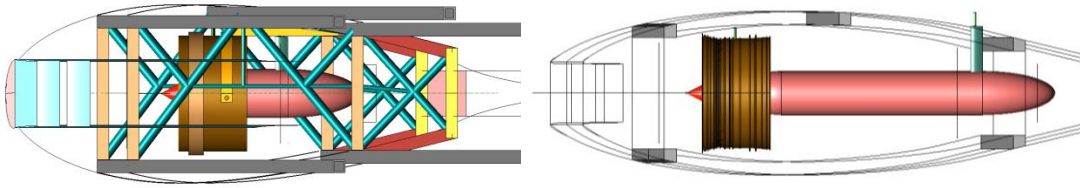

Figure 13: In-board fan-motor assembly using N+3 technologies, including superconducting motors (left), and scaled conventional technologies (right). (13)

The NASA SBIR studied and designed the structural layouts, aircraft weight buildup methodologies, and other aircraft design tools, but lacked any substantial aerodynamic analysis for the split-wing configuration, which happened to be a significant aspect of the design. Regardless, there were several interesting takeaways from the SBIR work, including sizing methods for number of fans vs. TOGW. See Figure 14.

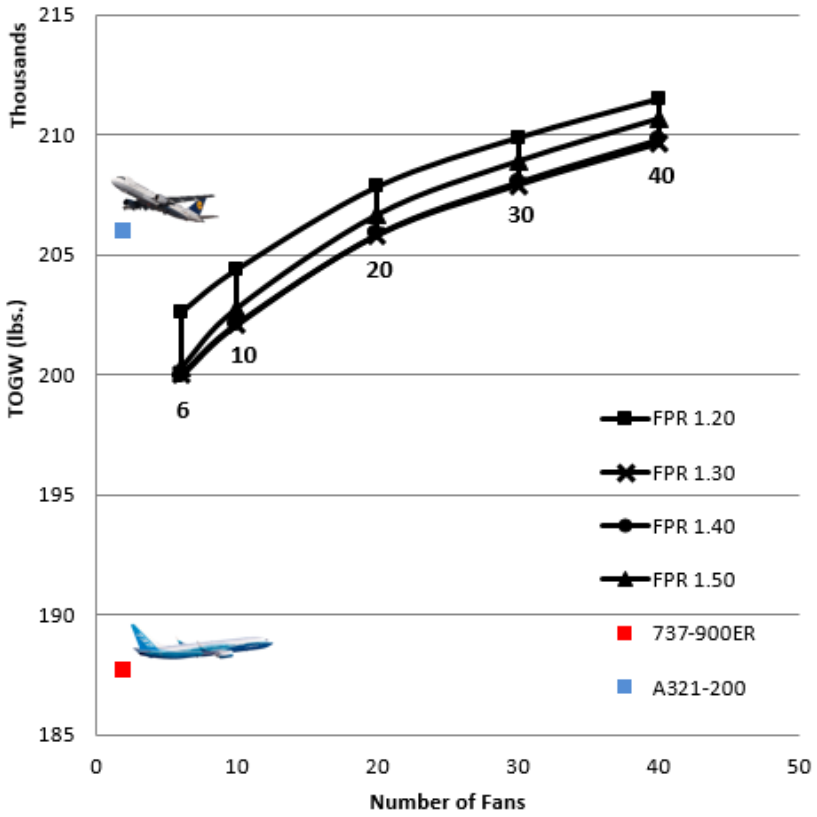

Figure 14: Fan Pressure Ratios (FPR) for varying number of fans and TOGW. [16]

The initial study looked at fan pressure ratios for a 2 turbo-generator, hybrid-electric propulsion configuration. The top-of-climb design thrust for the aircraft was 10900 lb. The study accounted for fans, fan frames, motors, generators, controllers, power cables, and turbine engines. Both current regional commercial replacement platforms are shown as well.

2.3 Split-Wing Aerodynamic Performance using Computational Fluid Dynamics

Currently, only a preliminary computational fluid dynamics model was applied to the split-wing configuration as part of a Phase I SBIR awarded to ESAero. Dr. Russ Cummings of the Air Force Research Laboratories performed the preliminary studies in a consultant capacity. Figure 15 and Figure 16 show the fan duct system investigated as part Dr. Cummings CFD modeling.

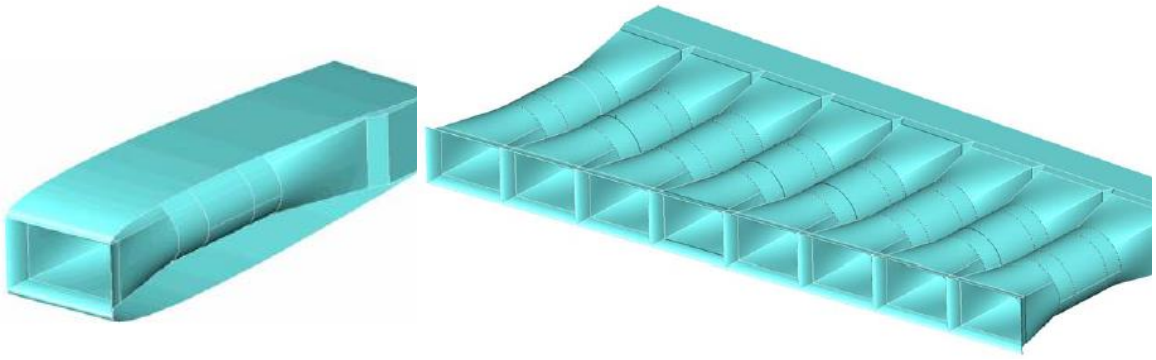

Figure 15: Most inboard fan duct (left) and fan duct network without fans or structure (left). [11,13]

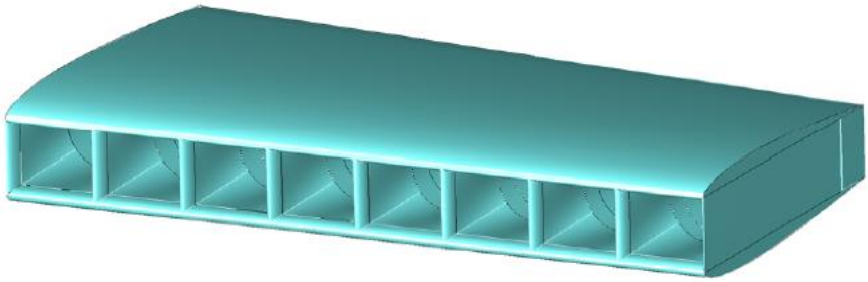

Figure 16: Trimetric View of Inboard Wing Section with airfoil included. [11,13]

A CFD analysis was performed for one engine of the inboard distributed propulsion architecture. Both 2-dimension and 3-dimension analyses were conducted using the unstructured Navier-Stokes flow solver Cobalt (from Cobalt Solutions LLC). The Spalart-Allmaras turbulence model was used for all flow predictions, and all boundary layers were assumed to be turbulent. The engine section consists of two NACA airfoils with ducting between to provide space for the fan / motor.

The baseline grid used for the proposed Phase I work was generated using a hybrid software approach. An unstructured surface grid was created in GridGen and exported as the baseline for the volume grid. The hybrid unstructured volume grid was generated by AFLR3, a code developed at Mississippi State University. The resulting baseline volume grid contains approximately 2 million nodes and 4.5 million cells (4 million prisms and 500,000 tetrahedra), as shown in Figure 17.

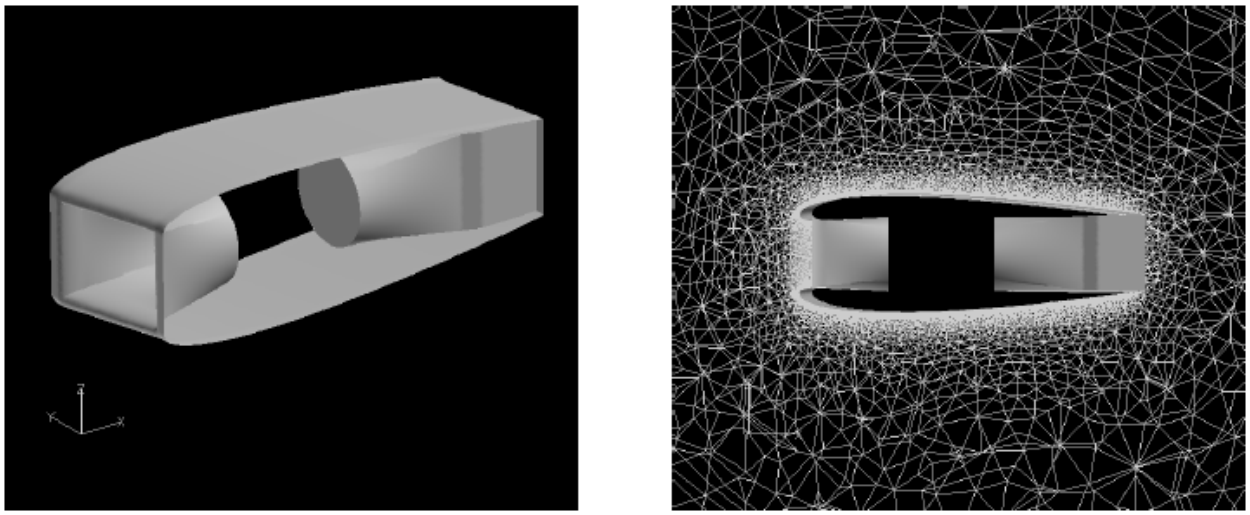

Figure 17: Surface geometry of single propulsion module and unstructured mesh around the geometry. [13]

The baseline grid was used to analyze the flowfield using the following boundary conditions: Modified Riemann invariants at all farfield boundaries, adiabatic no-slip (viscous) solid surfaces, symmetry plane to the left and right of the engine sections, sink with constant mass flow rate at engine inflow face, source with specified total pressure, total temperature, and Mach number at engine outflow face. Three basic cases were analyzed with the flow solver: Mach 0.65 at 30,000 ft, Mach 0.70 aft 30,000 ft and Mach 0.2 at 0 ft. Additionally, three angles of attack (α) were analyzed: $\alpha = 0^o$, 4^o, and 8^o.

The results for Case 1 are shown in Figure 18 and Figure 19; off-surface pressure and Mach number are presented for $\alpha = 0^o$, 4^o, and 8^o. The flow into the inlet for all three cases was smooth, with no flow separation present. As the angle of attack increased the upper surface of the wing developed a region of localized supersonic flow, terminating in a normal shock. At 8 degrees angle of attack the shock contributed to upper surface flow separation, leading to a stalled wing. These initial 2-D CFD solutions were also used as one method of verification of the tool provided in this work.

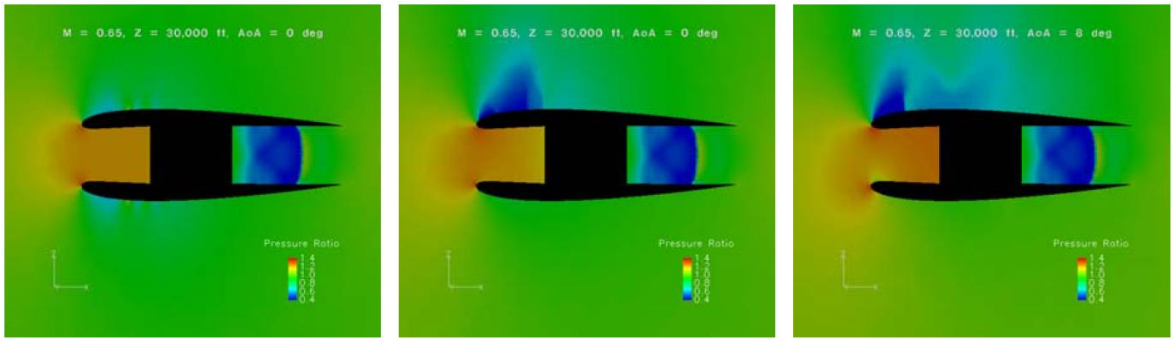

Figure 18: Off-surface Pressures for ∝ = 0 degrees (left), ∝ = 4 degrees (middle), and ∝ = 8 degrees (right). [13]

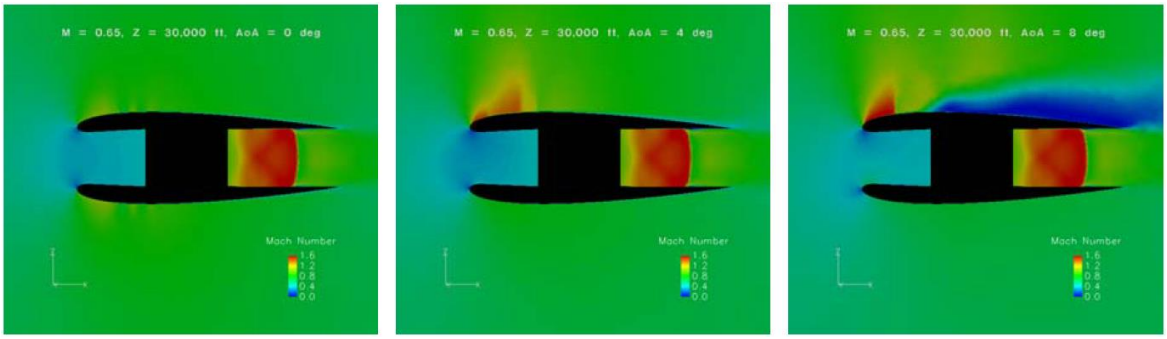

Figure 19: Off-surface Mach numbers for ∝ = 0 degrees (left), ∝ = 4 degrees (middle), and ∝ = 8 degrees (right). [13]

While this AFRL study did provide a template for the work completed as part of this thesis, there were several limitations that necessitated further investigation. As seen in Figures 18 and 19, the CFD analysis omitted all the propulsive devices and associated flow. While the outer flow was not affected, the inlet and nozzle flow was greatly altered due to this shortcoming.

The airfoil selected (NACA 0012) was split in two and separated with minimal shape considerations, especially for the nozzle section. Without a constrictive nozzle, this 2-D representation would provide minimal thrust and negatively affect the outer flow field. Additionally, no inlet considerations were made, providing no insight into how the shape of the inlet affected the outer flow.

2.4 Split-wing Structural Considerations

The split-wing configuration is a novel aerodynamic, propulsive, and structural configuration. Locating the propulsors inside the wing complicates the wing structural load paths. The standard spar / rib layout is no longer feasible for this design, leading to a full split-wing truss structure

capable of supporting the propulsors, housing the power and cooling lines, providing enough structural rigidity for wing bending, and fitting within the outer mold lines of the airfoil, all while keeping the weight to a minimum.

ESAero, working on a NASA SBIR project, developed a notional wing cross-section for split-wing. The design required for a majority of the propulsive weight of the distributed propulsion system to be located in the inboard wing section. Other conventional weight estimation methods were be used for the fuselage, empennage, landing gear, gear pods, outboard wing panels, and the turboelectric generator nacelle. The inboard wing structural components have a direct relationship to the number of fans and fan diameter. Figure 20 presents an inboard section rib cross-section with three spars in the upper inboard wing torque box and two in the lower torque box.

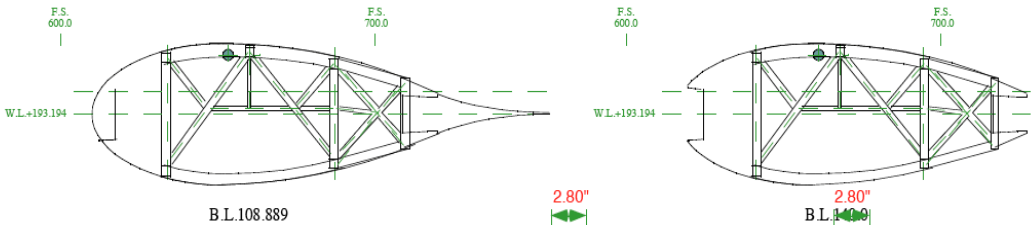

Figure 20: Inboard wing initial truss structure layout for ECO-150 N+2[11,13].

The baseline design for this thesis is based loosely on the geometry from Figure 20. 3-D structural considerations implemented as part of the ESAero effort included cooling and fuel lines, wing loading, material selection, spar sizing, and wing box sizing. These considerations would have to be considered as part of a full system, split-wing configuration.

2.5 NACA Wind Tunnel Testing

As a method of validating the computational results suggested in this thesis, wind tunnel data from National Advisory Committee for Aeronautics (NACA) was recorded as part of a World War II war report. These studies represent the closes actual wind-tunnel empirical analogy to the split-wing configuration proposed as part of this thesis. The then-confidential report looked into

inlet design for various cambered airfoils[34]. This report took larger thickness airfoils and tested them versus a narrow inlet version of the same outer mold-lines, as shown in Figure 21.

Pressure distributions were recorded for basic airfoil sections and inlet sections. These test arrangements and pressure data represent another method of verification and validation of the tool presented in this work.

The NACA report investigated three airfoil types: symmetric airfoil, medium-camber airfoil, and high-camber airfoil. The symmetric airfoil is of particular interest as it most closely matches the baseline design presented in this thesis. Mach numbers investigated included: 0.2, 0.4, and 0.65. Additionally, multiple inlet velocity ratios and angle of attacks were used during their investigation.

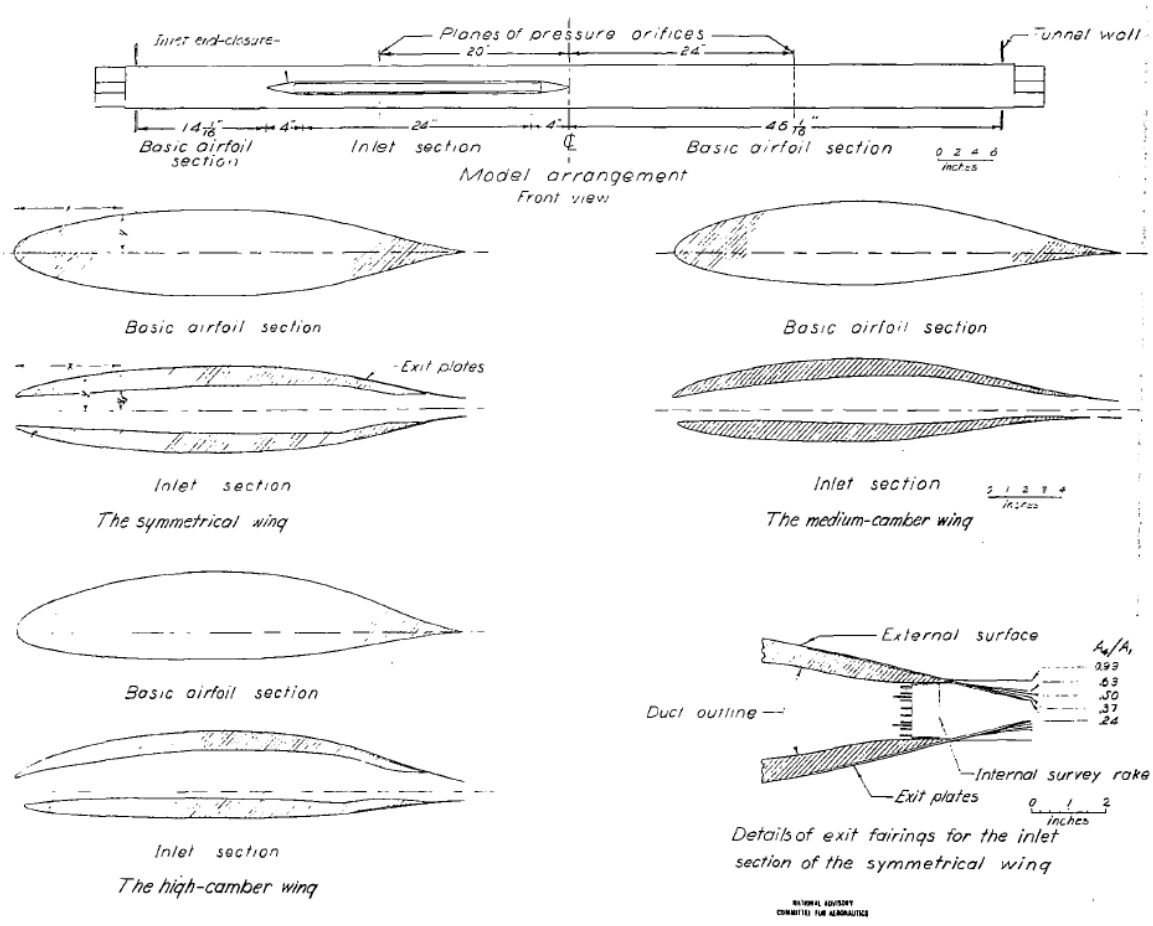

Figure 21: NACA Wartime Report wind tunnel setup and airfoil depictions.[34]

Figure 21 demonstrates the NACA test arrangement, airfoil sections (basic airfoil sections), and inlet sections.

Figure 22 shows pressure distributions for the upper and lower surfaces of inlet sections and their associated 'non-inlet' airfoil for each Mach number. For each case, there is a precipitous decrease in pressure coefficient at the leading edge for the inlet sections. Pressure distributions are shown for the inlet section of the three wings at angle of attack (α) of 0º and inlet velocity ratio (V_1/V_0) of 0.5.

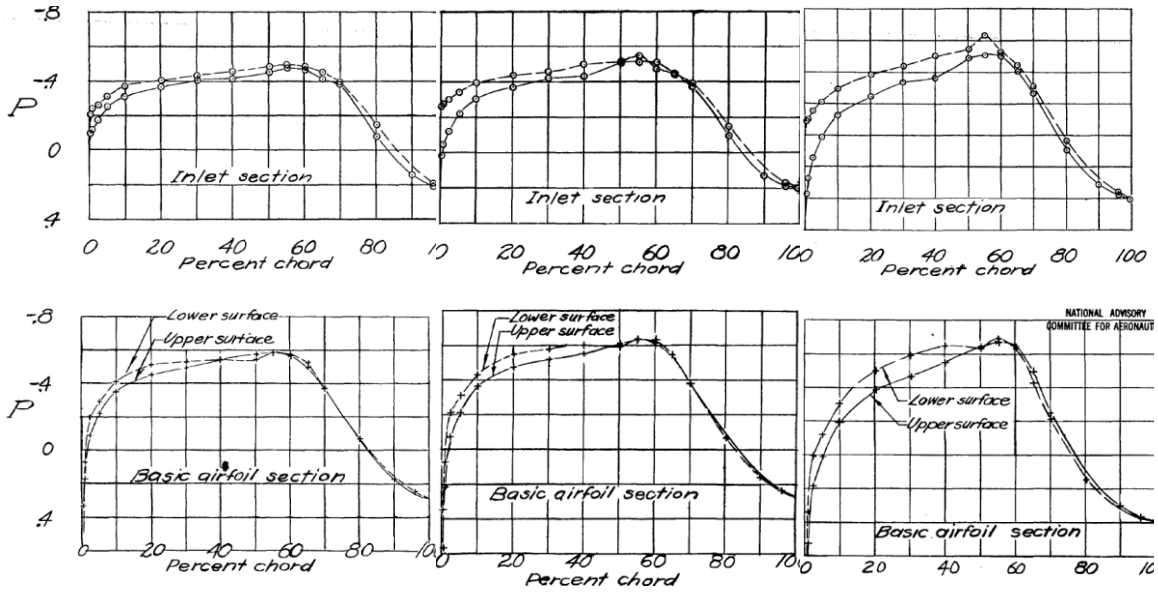

Figure 22: NACA pressure distributions for the symmetrical wing inlet sections (top row) and basic airfoil sections (bottom row) for M = 0.2, 0.4, and 0.65 from left to right, respectively[34].

Figure 23 shows the inlet pressure ratios for both the upper and lower surfaces for chord distances 0 to 30% chord with varying angles of attack (α) and Mach numbers. These data were digitized and used as verification and validation.

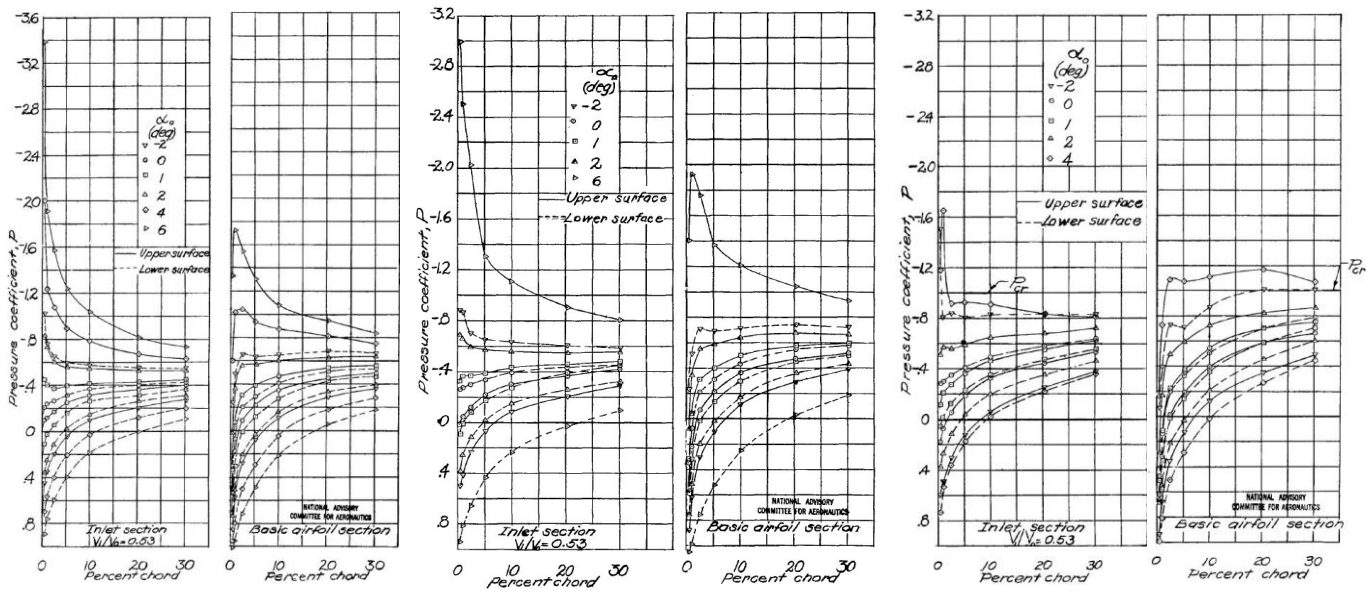

Figure 23: NACA test data of pressure coefficients for symmetrical wing inlet and basic airfoil sections (M = 0.2, 0.4, and 0.65 from left to right, respectively)[34].

Another similar study conducted by the National Advisory Committee for Aeronautics illustrates the preliminary investigations into leading edge inlet designs[40]. This study, dated July 1942, tested using flexible model to derived airfoil shapes including thickness, camber, leading-edge radius, and size of leading edge. The purpose of this study was to determine a range of C_L for high-speed and cruising flight using an inlet. There were numerous shapes considered, including symmetrical inlets used as a verification and validation tool. The specific shapes used in this thesis were: Shape 7, Shape 8a and 8b, Shape 9, and Shape 10.

> *"Shapes show no substantial increase in drag over that of normal low-drag type sections having minimum pressure at the same position along the chord."*[40]

Low-drag airfoil sections have been developed with openings in the leading edge as large as 41.5% of the maximum thickness. However, no conclusions could be drawn due to measurement inaccuracies for maximum lift characteristics.

> *"Leading edge of the wing has proved to be a convenient location for the entrance to air ducts. This location is potentially efficient because the air can be brought to rest at this point without loss of total pressure."*[40]

Figure 24 depicts the pressure distribution for the upper and lower surfaces of Shape 7 at takeoff conditions.

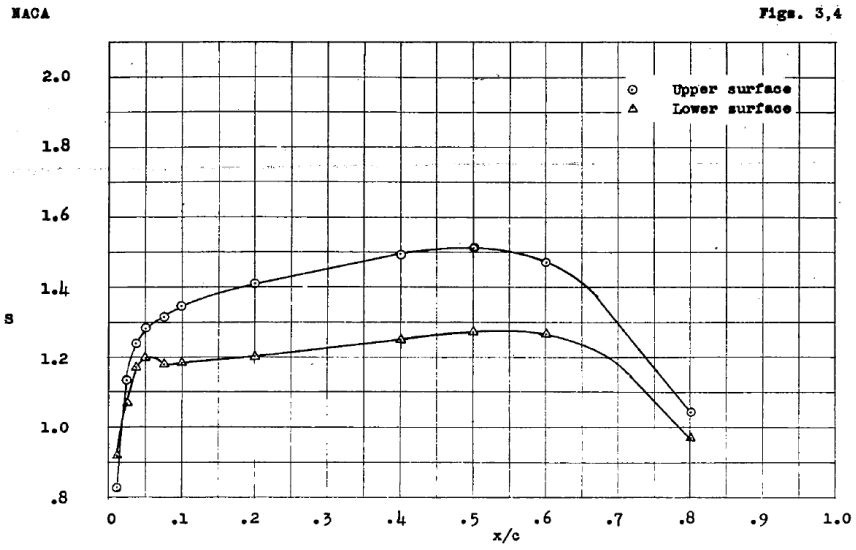

Figure 24: Pressure distributions for "airfoil shape 7", cambered for $c_l = 0.2$ with sharp leading edge. ($\alpha = 0^o$; $v_n/v = 0.426$; $A_t/A_n = 0.439$, $Re = 2.02 \times 10^6$). [40]

The Shape 8 study had two leading edge radius curvatures (Shape 8a and 8b). Shape 8a had a 1/32" leading-edge radius and 8b had a 1/16" leading-edge radius. The inlet cross-section and respective coefficient of pressure distributions are shown in Figure 25. Figure 26 demonstrates the change in sectional lift coefficient (c_l) for Shape 8a, 8b (left), and Shape 9 (right).

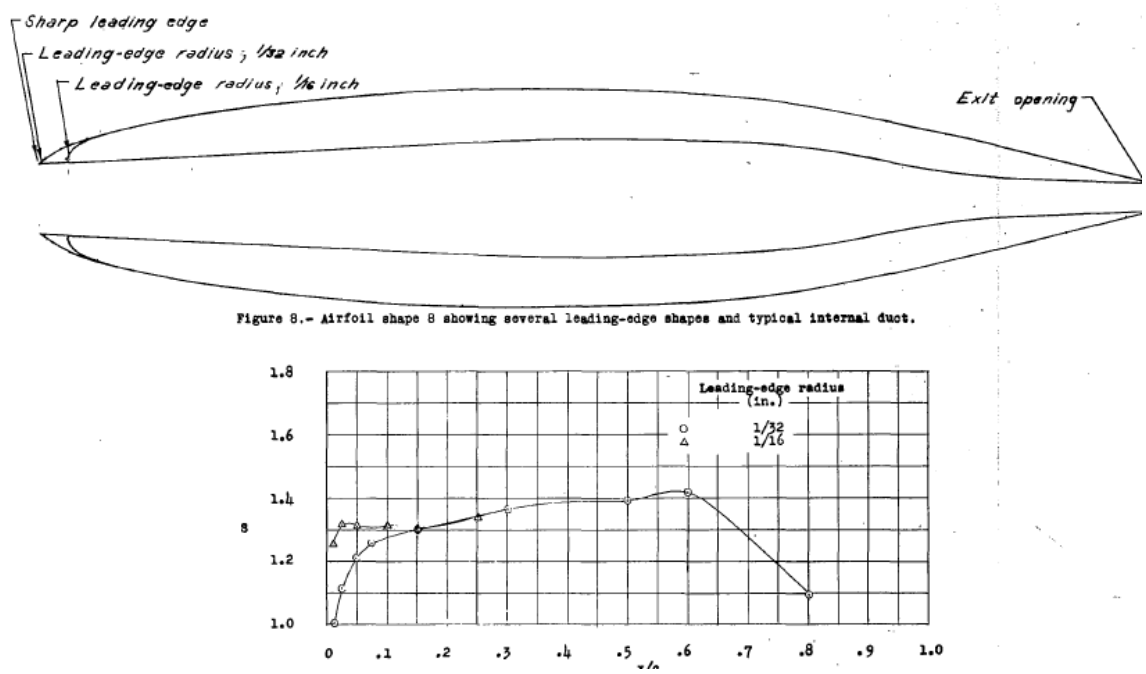

Figure 25: Pressure distributions for "airfoil shape 8 ", cambered for c_l = 0.2 with sharp leading edge. ($\alpha = 0^o$; $v_n/v = 0.426$; $A_t/A_n = 0.439$, Re = 2.02 x 10^6). [40]

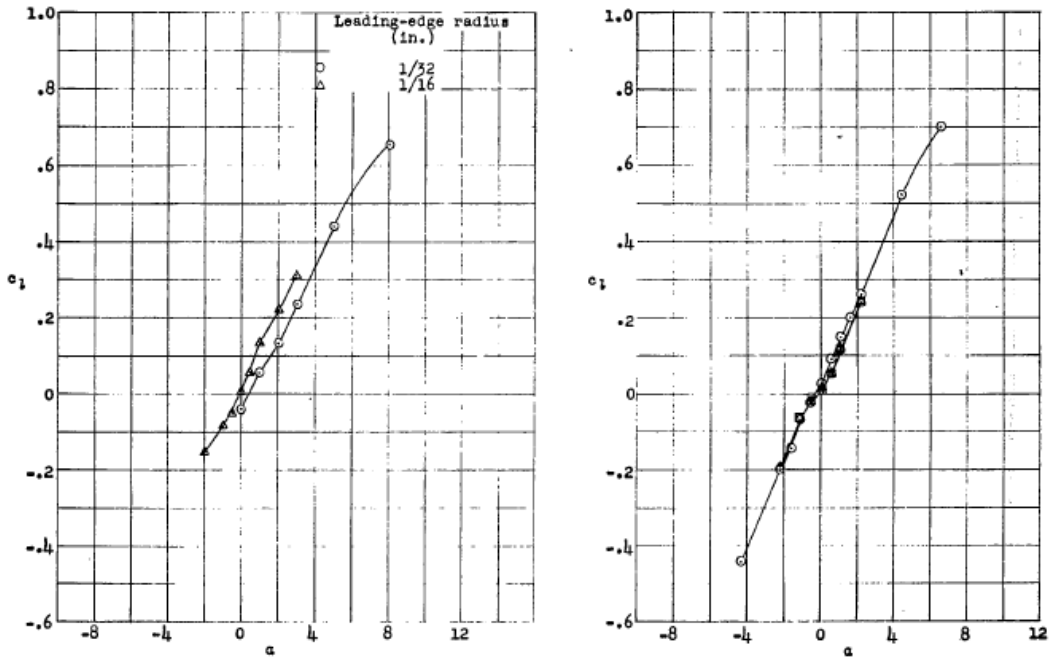

Figure 26: (L) c_l for airfoil shape 8 with small and large LRR (A_t/A_n = 0.439, Re = 2.02 x 10^6), (R) c_l for airfoil shape 9 with various flow rates (Re = 6.43 x 10^6). [40]

These NACA wind tunnel tests are a key verification method for this work. These results are paired with the results from this thesis in Section 4.3. The purpose of these studies was to investigate methods for reducing the adverse leading edge pressure distributions for WWII fighters

and was never intended to be an inlet shape study; therefore, no propulsive systems (i.e. engines, motors, fans, etc.) were considered. Additionally, the narrow inlet sizes also reduced the effectiveness for using these Wartime Reports as methods of verification and validation. Unfortunately, no other pertinent studies on this design were discovered.

2.6 Split-Wing Inlet Sizing Methods

Several small businesses including ESAero have investigated empirical methods for inlet sizing based on circular inlet geometry and applying shape change algorithms to account for the rectangular nature of the split-wing. These tools provide a useful stepping stone to the further investigation of this thesis.

Typical nacelle inlets are based on circular inlet geometry and a diffuser with increasing area leading to the fan inlet. A typical inlet design, shown in Figure 27, demonstrates the 3-dimensionality of the inlet geometry.

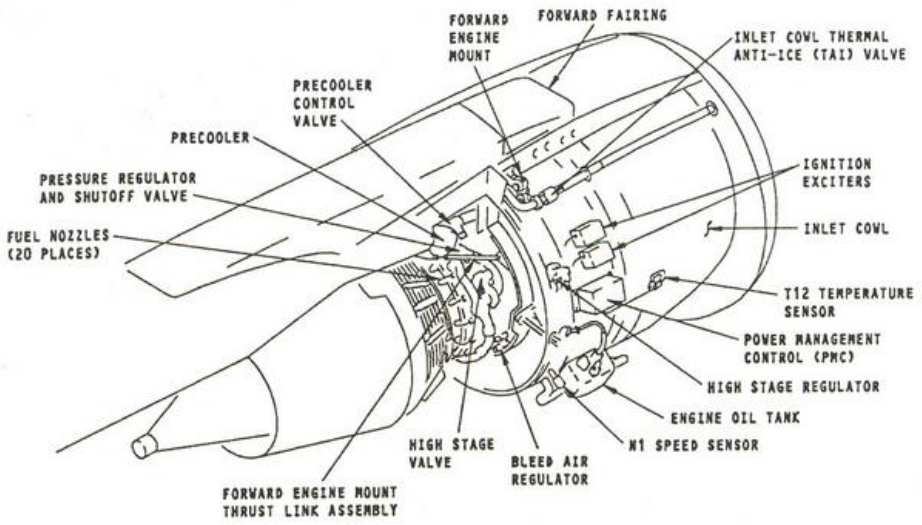

Figure 27: CFM56 Arrangement, showing 3-dimensionality of inlet, courtesy of CFM International.[23]

According to research, the boundary layer should maintain a constant shape, even though the boundary layer thickness will increase as the flow progresses down the diffuser [10]. For circular inlet geometries, Kline demonstrated that for incompressible flows, the diffuser geometry is dependent on diffuser angle and the ratio of diffuser length to throat diameter.

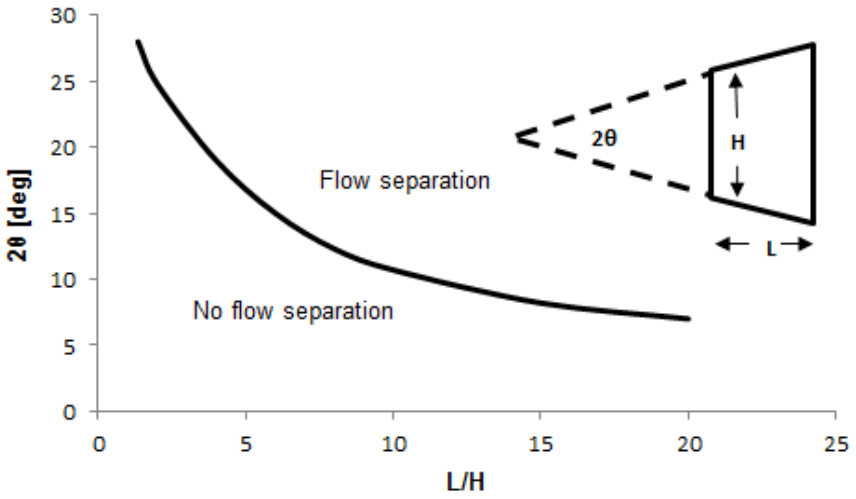

Figure 28: Flow separation limits in 2-dimensional straight-walled diffusers.[23]

These studies are only partially useful for the split-wing geometry, as the much of the physics for flow separation is based on the circular geometry.

As part of another NASA SBIR work, ESAero has developed a first-order split-wing inlet sizing methodology detailing their inlet analysis capability. Described here is a brief description of the findings and inlet sizing relationships. However, the significant drawback to this analysis is that the empirical data refers to circular inlets and not rectangular inlets as defined by the split-wing design.

Initially, the ratio of Mach numbers for freestream (M_0) and throat (M_1 or M_{th}) determines inlet pressure ratios and speed characteristics. Figure 29 shows the difference between supercritical and subcritical flow into the inlet. The 2-D circular area in front of the inlet that encapsulates the all the air that will pass through the inlet but negating all air destined to flow over / under the inlet is known as the capture area ($A_{capture}$). The area at the lip of the inlet is known as the throat area (A_{th}); technically throat area and lip area can differ for large leading edge radii, but those geometries we're considered.

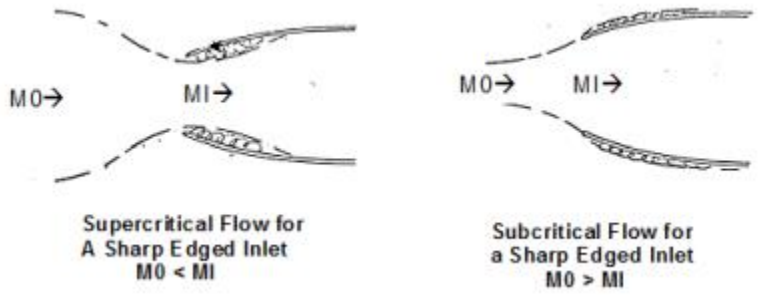

Figure 29: Graphical depiction of supercritical and subcritical inlet conditions.[6]

Figure 30 focuses on the subcritical flow, as it pertains to the speed range for regional airliners. However, the inlet shown is known as a sharp inlet, similar to the NACA symmetrical wing shown in Section 2.5. The blue areas above and below the upper and lower inlet surfaces is assumed to be turbulent flow. The more blunt inlet shapes have different Mach number and pressure distributions and direct comparison is rough.

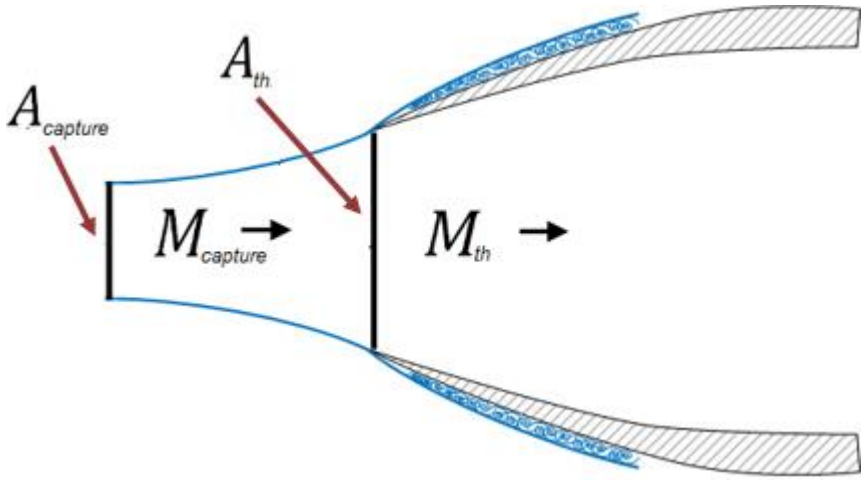

Figure 30: Subcritical flow for a sharp edge inlet ($M_{capture} > M_{th}$).[13]

The methodology developed by ESAero utilized Crosthwait's accounts for nominal diffuser pressure ratio as well as takeoff and low speed augmentations[6]. The diffuser represents the perpendicular surface between the throat and the fan face. The diffuser pressure ratio (pressure ratio loss from throat to fan) or $\frac{P_2}{P_{th}}$ is independent of sub- or supercritical conditions. It can be calculated as shown in Equation 1 (Eq. 1).

$$\frac{P_2}{P_{th}} = 1 - \left[K_D K_{M_{th}} \left(1 - \frac{A_{th}}{A_2}\right)^2 \left(1 - \frac{p_{th}}{P_{th}}\right)\right] \qquad \text{Eq. 1}$$

The diffuser total pressure loss factor (K_D) is then determined by the boundary layer thickness at the throat and diffuser expansion angle. The assumed boundary layer thickness at the throat $(\delta^*/r)_{th}$, is 0.010. See Figure 31.

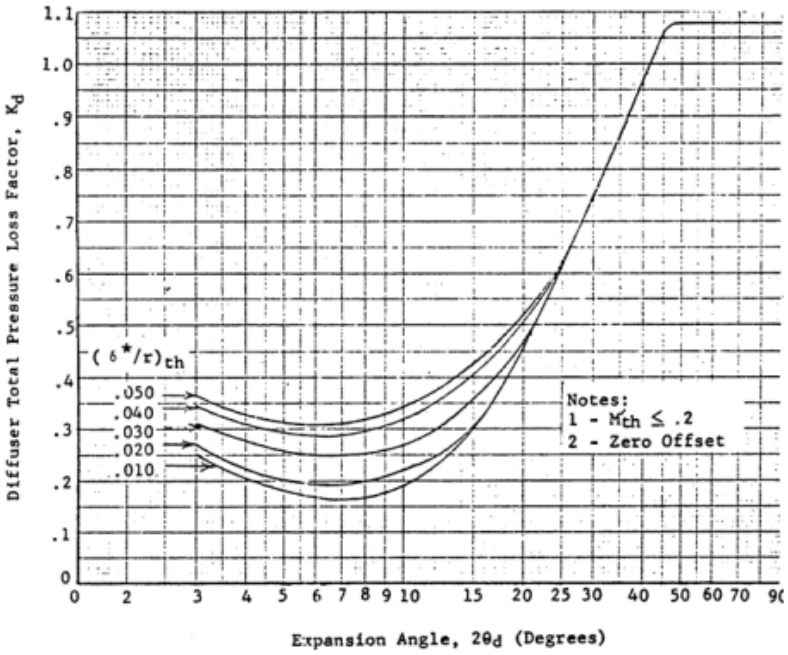

Figure 31: Diffuser total pressure loss factor as a function of expansion angle and throat boundary layer.[6]

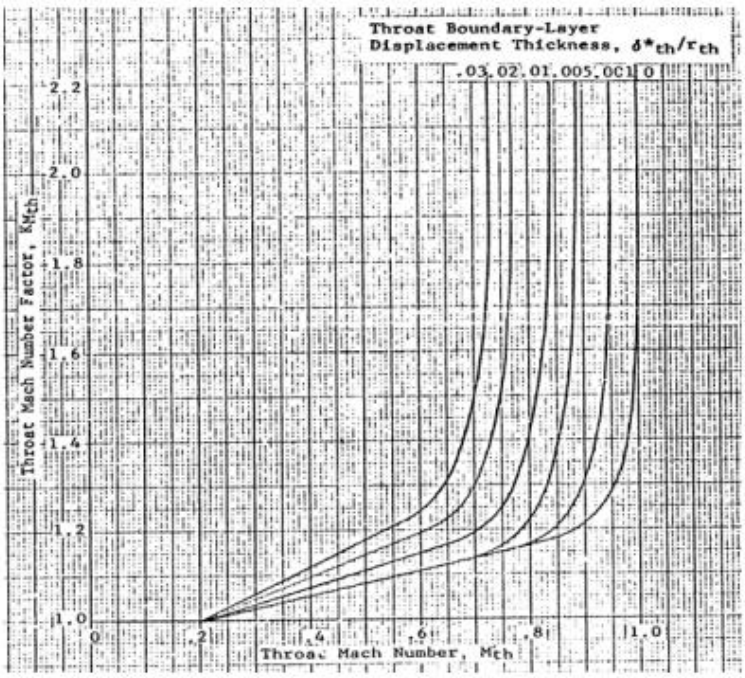

Figure 32: Throat Mach Number Factor (K_{Mth}) as a function of Throat Mach Number (M_{th}) and throat boundary layer.[6]

Figure 32 depicts the throat Mach number (K_{Mth}) as a function of throat Mach number (M_{th}) and throat boundary layer. These empirical relationships were developed into a first-order inlet performance tool. Some interesting finding include lip radius ratio (LRR) relationships for local Mach number vs. inlet pressure ratios and additive drag [lbs]. See Figure 33. In the lower graph, Area Ratio refers to the ratio of throat area to fan area (A_{th} / A_2).

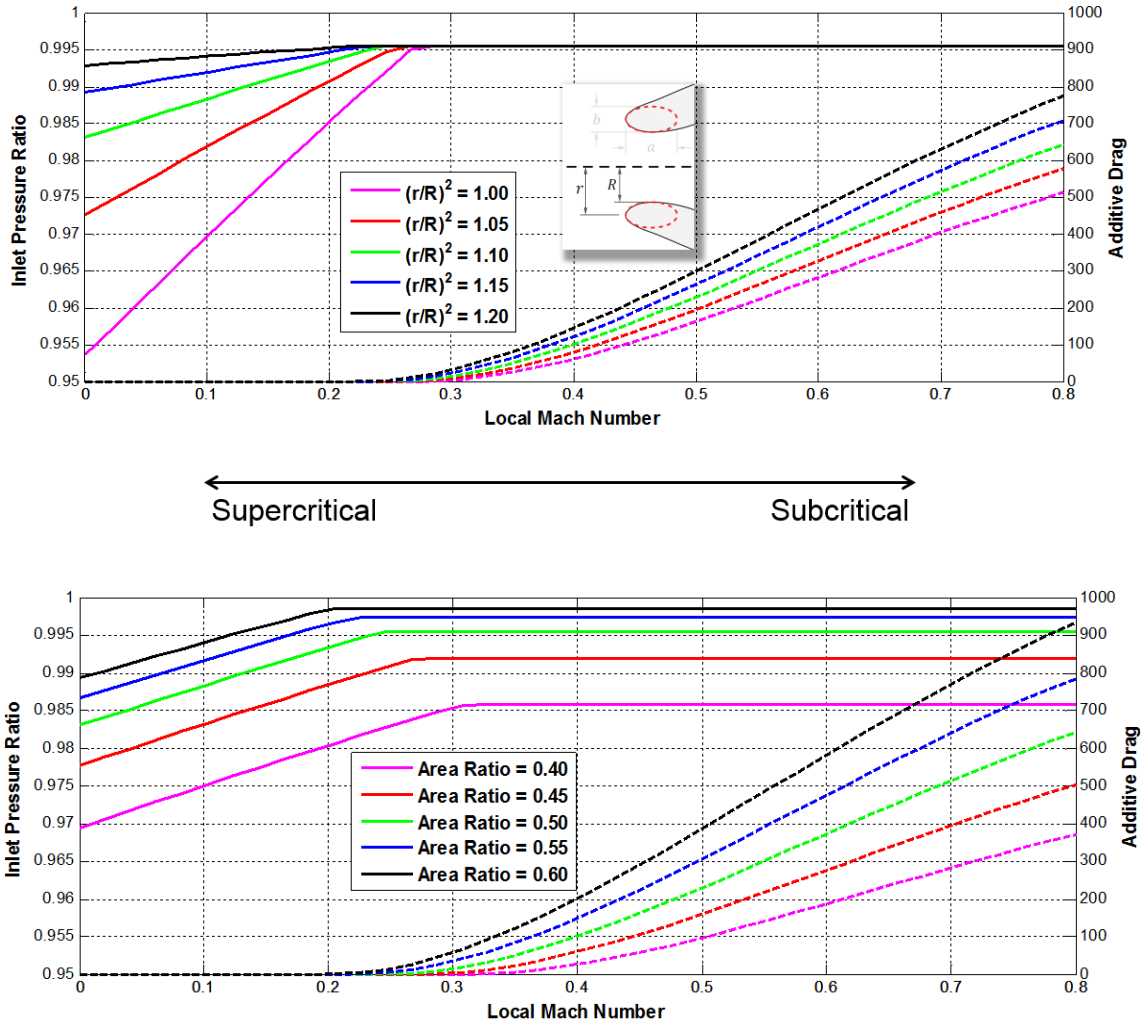

Figure 33: Inlet pressure ratio and additive drag [lbs] for varying LRR. (10)

These studies were effective in providing notional shape characteristics for a split-wing configuration with several limitations, including: empirical trends used for the analysis were based on circular inlet designs, only a single outer airfoil was considered, and only a single throttle / mass flow rate was considered.

3. Methodology

3.1 Hypothesis

The split-wing configuration will provide comparable aerodynamic behavior to either over-wing or under-wing configurations, as well as provide unique benefits including structural, systems integration, and controllability. The split-wing design will provide powered lift capability similar to a blown, under-wing design, while capturing improved efficiency similar the boundary layer ingestion methods employed by the over-wing design.

While not investigated in this study, wingtip propulsors could also be used with the split-wing design to alleviate the adverse wingtip vorticity drag.

3.2 System Sizing

The goal of this thesis was to produce a split-wing design tool for various inlet geometries. The baseline inlet design originated from an ESAero 2010 NASA SBIR study[11]. The notional airplane was a cryogenically-cooled, turbo-electric distributed propulsion (TeDP) B737 replacement aircraft. A proposal for work through Air Force Research Lab (AFRL) by Dr. Russ Cummings continued the investigation, providing notional CFD on a rudimentary inlet design (see Figure 15 through Figure 19). The limited CFD was ultimately inconclusive as to the effectiveness of the split-wing configuration. This study investigated several more aspects of the split-wing design, pulling from old NACA reports, engine nacelle sizing methods, and utilizing computational fluid dynamics (CFD), all while providing notional motor sizing and improved inlet flow calculations.

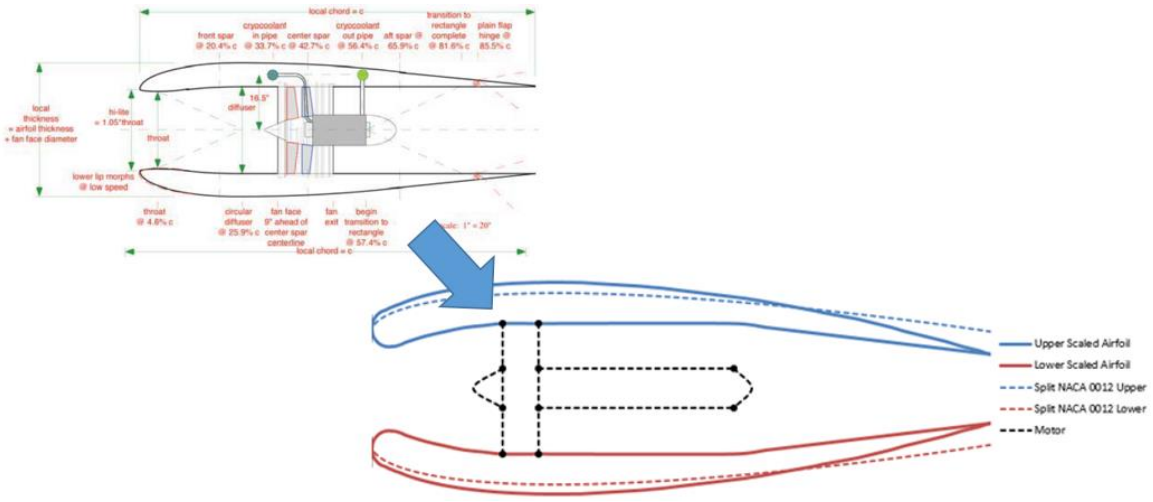

Figure 34: Converted ESAero Split-Wing Design into Rubberized Model.

The 2-D cross-section of a split-wing electric distributed propulsion configuration used in this analysis consisted of two halves of an airfoil, a fan, and an electric motor. Initially a NACA 0012 symmetric airfoil was split from leading to trailing edge and separated by a distance equal to the diameter of the motor divided by the hub-to-tip ratio of the fan; this geometry assumed the diameter of the motor was equal to the hub diameter of the fan. The original baseline and subsequent cross-section for this study are shown in Figure 34.

Cruise was selected as the primary design flight condition used for this study. Sizing for cruise and not takeoff or top-of-climb conditions reduces the power and thrust requirements for the turbine engines; the additional power would be provided by a battery, supercapacitor, flywheel, or fuel cell. This architecture model has been employed by several companies and government agencies as a pathway to improved fuel / energy consumption.

Current state-of-the-art (SOTA) electric machinery reduces the effective cruise speed and/or range. Flying near Mach 0.78 (current regional airliner cruise speed) would require significantly larger electric equipment and cabling, leading to a design that would not be able to complete the prescribed mission. Reducing cruise speed has been seen as the current fix until battery / fuel cell technologies improve.

With slower cruise speeds currently necessary for TeDP designs, the following design considerations were made:

Table 3: Fan design parameters.

Parameter	Value
Altitude	35,000 feet
Cruise Speed (Mach)	0.65
Notional Design Inputs for HAPSS*	-
Fan Size	25 inches
Pressure loss in inlet and nozzle	1%
Fan efficiency	95%
Nozzle expansion	Optimal
Hub-to-tip ratio	0.30

* HAPPS[16] was run for a notional TeDP B737 design

The fan map produced by HAPPS using the parameters listed in Table 3 is shown in Table 4. The maximum power for the motors was 800 hp. This assumes a distributed bed of fan / motor assemblies (on the order of 16-20 propulsor groups total). The percent power correlates with throttle setting. The mass flow rates were matched through fan outlet and fan inlet pressure boundary conditions during the CFD study.

Table 4: Motor and fan on-design specifications from HAPSS.

% Power	Input Power	Mass Flow Rate		Inlet Throat Area	Throat Distance	Nozzle Exit Area		Net Thrust	Fan Pressure Ratio
-	hp	lbm/s	kg/s	ft^2	in	ft^2	in	lbf	-
100%	800	55.72	25.27	3.10	21.12	2.08	17.31	511.92	1.35
80%	640	45.49	20.63	3.10	21.12	2.08	17.33	416.83	1.36
60%	480	42.23	19.15	3.10	21.12	2.04	17.16	320.55	1.28
40%	320	37.70	17.10	3.10	21.12	1.95	16.76	219.10	1.21
20%	160	30.64	13.90	3.10	21.12	1.73	15.79	111.29	1.12

The electric motor was the design driver for this trade study. There are several constraining technologies, including cabling requirements, motor / generator size, weight, and cooling requirements, battery requirements and electrical power bus network requirements. However, the motors powering the fans were driving this analysis, whereas the other technologies had no direct impact on the inboard wing design. Those omitted systems would absolutely need to be integrated into a more thorough point design, but that diverges from the scope of this study.

With a desired power profile, a motor can be scaled using the motor diameter and motor length. Per discussions with David Calley, formally of Motor Excellence, the torque for a motor scales as with diameter (Dia) squared and proportional to length,

$$\tau \propto Dia^2 \quad \tau \propto Length \qquad \text{(Eq. 2)}$$

Since the torque is proportional to the power of a motor, by base speed (excluding low and high RPM ranges), the power of the motor can roughly be scaled with torque.

Currently, there are no motors in the applicable power regimes that are light enough to be useful for aerospace applications, so extrapolation of motor technology was used for this design trade study. Figure 35 shows a survey of current state-of-the-art (SOTA) electric motor power and weights. Additionally, Figure 35 shows maximum or peak power vs. mass; continuous speed is more realistic in terms of heating and power load.

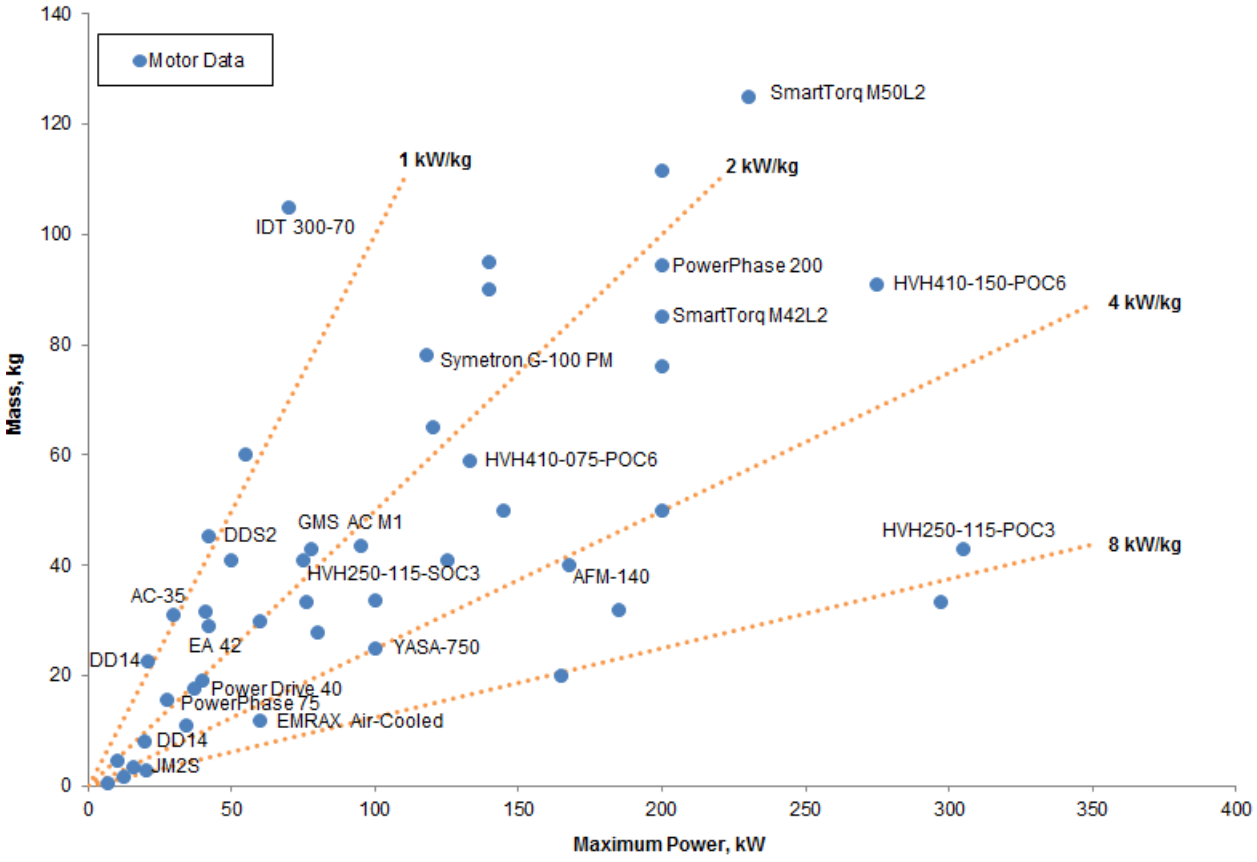

Figure 35: Current state-of-the-art high power-to-weight electric motor survey.

The Remy International HVH-250-115-POC3 was chosen as the motor to be scaled for this study. It has an attractive power to weight and is still a large motor, providing more confidence in scaling up to ½ MW range.

Table 5: Motor scaling results for baseline design.

Motor Sizing		
Scaled from: Remy Int. HVH-250-115-POC3		
Hub-to-tip ratio	0.30	-
Chord	127.5	inches
Motor diameter	7.29	inches
Motor length	38.16	inches

A TeDP design with 20 motors (10 on inboard section of each wing) was used requiring 800 horsepower (597 kW) at maximum power condition: takeoff. The scaled motors had the following characteristics, which were used in determining the cross-sectional geometry shown in Figure 34.

Three data sources were considered: two NACA Wartime Reports and computational fluid dynamics (CFD). The NACA reports were flight research projects investigating the usefulness of leading edge inlet design for wartime applications. Both tests were conducted using a wind tunnel and scale model. Since these two studies represent the only experimental data available, the computational methods were compared against the NACA reports, providing degrees of confidence for each method and flight condition.

The NACA symmetrical airfoil study (airfoil shown in Figure 21) was particularly useful as it tested both baseline and inlet sections, with the inlet sections retaining the outer mold-lines. This comparison provided a notional inlet offset, as the percent difference of the two, for a symmetrical inlet examined at takeoff, climb, and cruise conditions (M = 0.2, 0.4, and 0.65, respectively).

The CFD analysis used viscous flow. Fluent by ANSYS was used as the physics engine and ICECFD was used as the meshing software. Several turbulence models, including Spalart-Allmaras (1 equation), k-ε (2 equation), k-ω (2 equation), and SST with γRe_θ transition model (2 equation) were used, with minimal difference and no substantive trends, but with dramatically

different run times; for this purpose, Spalart-Allmaras was used. Several cases were run with half the node count in order to estimate the exact discretized solution using Richardson's Extrapolation method. The discretization offset was then applied to the other CFD runs for varying flight conditions. The CFD results were also compared to the NACA wind tunnel data. Both error estimations were applied to the CFD results.

3.3 Rubberized Split-Wing Cross-Section

With the motor sized and the airfoil split, some additional functionality was provided. Several parameters were added, including Lip Radius Ratio (LRR), inlet length, airfoil thickness, motor diameter, motor length, and fan diameter. Additionally, inlet throat diameter and nozzle diameter were also included, but as dependent variables. The rubberized cross-section provided multiple inputs for CFD batch runs. Discussed later in Section 5.5, the rubberized cross-section was converted to a supercritical airfoil shape and additional features were included. Those efforts represent future work considerations.

3.4 Inlet Design Tool Trade Space

The trade space for the "Inlet Shape Considerations for Split-Wing Electric Distributed Propulsion" is shown in Table 6. The Symmetrical Basic and Symmetrical Inlet, the Medium Camber Basic and Medium Camber Inlet, and the High Camber Basic, and High Camber Inlet come from the NACA high-speed investigation of low-drag wing inlets, shown in red[34]. In green, the CFD cases are shown. Four additional geometries from the NACA low-turbulence investigation for admitting air at the leading edge were used, shown in purple[40]: Shape 7, Shape 8, Shape 9, and Shape 10 (Figure **25** shows the cross-section of Shape 8). These geometries were tested between Reynolds' Numbers 2.00×10^6 and 6.43×10^6. The full tradespace includes Reynolds' Numbers between 1.80×10^6 (M = 0.2, 0kft) and 1.93×10^7 (M = 0.65, 30kft). There are four test cases that are particularly useful for comparing the various tools:

1) $\alpha = 0^o$, M = 0.2, alt = 0 kft, Re = 1.80×10^6
2) $\alpha = 0^o$, M = 0.65, alt = 30 kft, Re = 1.93×10^7
3) $\alpha = 4^o$, M = 0.2, alt = 0 kft, Re = 1.80×10^6

4) α = 4°, M = 0.65, alt = 30 kft, Re = 1.93 x 10^7

These cases provide at least one geometry from the NACA high-speed investigation, and at least one CFD case for comparison.

Table 6: Split-wing electric distributed propulsion inlet design tradespace.

Inlet Shape Considerations for Split-Wing Electric Distributed Propulsion Tradespace														
Mach Number (M)	Reynolds Number (Re) x 1,000,000	Angle of Attack (α) -2°	0°	1°	2°	2.5°	3°	4°	5°	6°	7.5°	8°	9°	10°
0.20	1.80	A1, A2	A1, A2, A3, C1, C2	A1, A2, A3	A1, A2, A3			A1, A2, A3		A1, A2, A3		C2		
	2.00		B2											
	2.02		B1											
0.40	5.45	A1, A2, A3	A1, A2, A3	A1, A2, A3	A1, A2, A3			A3		A1, A2, A3				
	6.43		B3, B4											
0.60	7.15	A2, A3	A2, A3	A2, A3	A2, A3									
0.65	7.43	A1	A1, A2, C1	A1	A1			A1, C1						
	19.30		C2, C2a, C2b, C2c, C2d, C3, C3a, C3b, C3c, C3d			C2	C3, C4		C2	C3, C4	C2		C3, C4	C2

A1: NACA Symmetrical (inlet & base)	B1: NACA Shape 7 (inlet only)	C1: CFD Symmetrical (inlet only)
A2: NACA Med Camber (inlet & base)	B2: NACA Shape 8a & 8b (inlet only)	C2: CFD Baseline (inlet only)
A3: NACA High Camber (inlet & base)	B3: NACA Shape 9 (inlet only)	C2a: CFD Baseline 80% Throt (inlet only)
	B4: NACA Shape 10 (inlet only)	C2b: CFD Baseline 60% Throt (inlet only)
		C2c: CFD Baseline 40% Throt (inlet only)
		C2d: CFD Baseline 20% Throt (inlet only)
		C3: CFD toc 9 (inlet only)
		C3a: CFD toc 9 80% Throt (inlet only)
		C3b: CFD toc 9 60% Throt (inlet only)
		C3c: CFD toc 9 40% Throt (inlet only)
		C3d: CFD toc 9 20% Throt (inlet only)
		C4: CFD toc 13 (inlet open)

3.5 NACA Symmetrical Airfoil Methodology

The NACA Wartime Report “High-Speed Investigation of Low-Drag Wing Inlets” symmetrical airfoil is shown below (left) and in Figure 21. The inlet was streamline with very small lip radii and throat ratio (ratio of throat distance to total thickness). One the right side of Figure 36 is the CFD mesh for measuring CFD inaccuracies. As shown later in Figure 42, the CFD compared very favorably for this geometry.

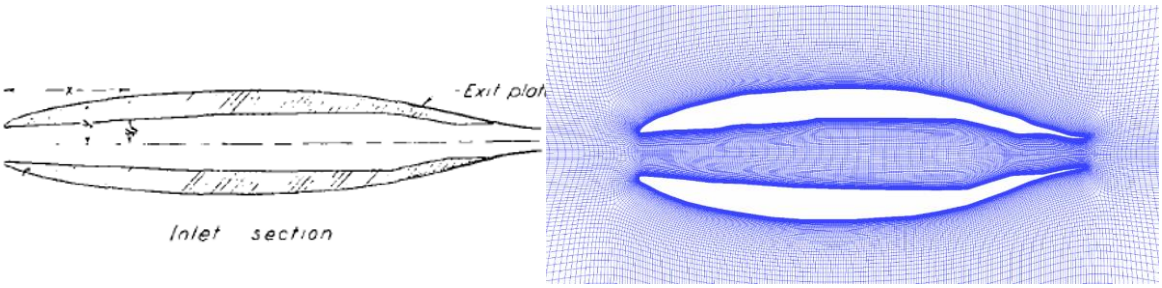

Figure 36: (left) NACA Wartime Report symmetrical inlet airfoil section[34] and (right) associated CFD mesh.

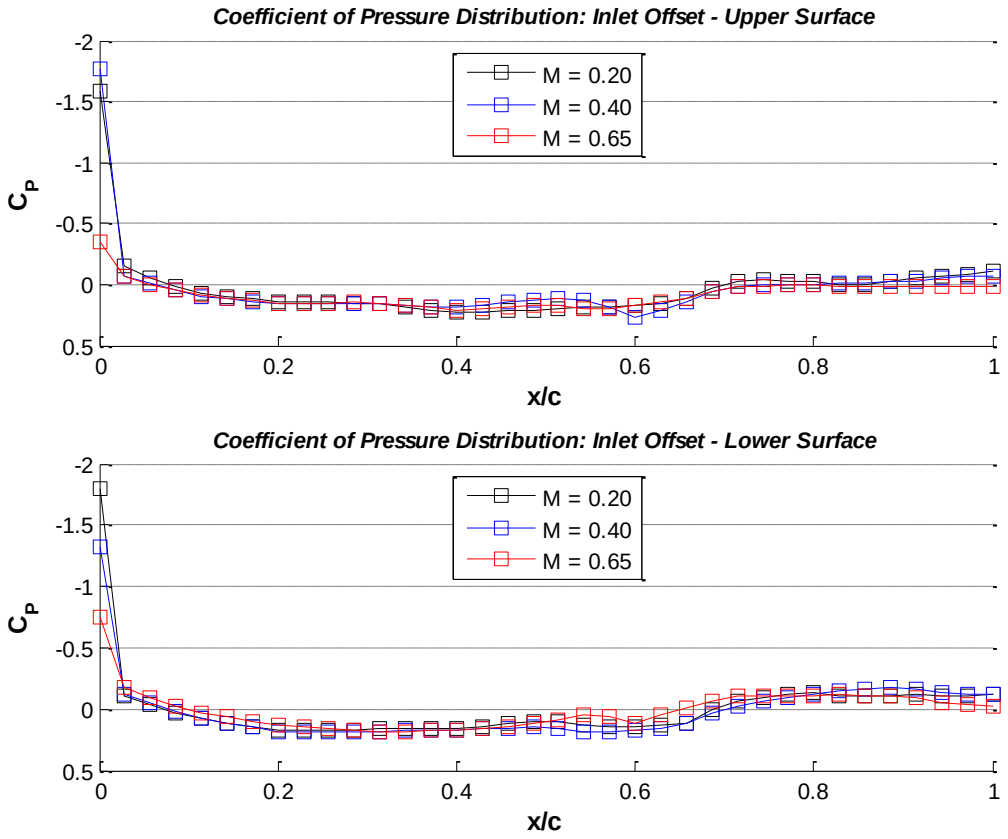

Figure 37: NACA Wartime Report symmetrical inlet offsets for M = 0.20, 0.40, and 0.65. [34]

As part of the NACA Wartime Report study, both an inlet geometry and a basic 'standard airfoil' were conducted in tandem. The resulting difference was the 'Inlet Offset', denoting the aerodynamic contribution from adding the inlet to a standard airfoil for multiple Mach numbers. As

seen in Figure **37**, the only perceptible change occurs at the inlet / leading edge and the nozzle / trailing edge, which is expected. The NACA report was digitized and interpolated into a set number of points to align with the other data sources.

3.6 CFD Methodology

The CFD analysis furthered the initial study by Dr. Russ Cummings during the unfunded Phase II SBIR proposal. Due to system complexity and scope, only 2-D CFD analyses were conducted for this study, limiting the overall effectiveness of the results. Additive drag, scavenging / starving of ducted fans due to changes in dynamic pressure to adjacent ducted fans must be considered for a more robust point designs. This study concentrated on a 2-D cross-section, extrapolating the flow physics along the extruded inboard wing. The goal of the CFD analysis is to provide design relationships for various inlet design parameters for preliminary aircraft configuration.

Previous computational techniques have been used to model ducted flow and can provide faster results for less cost than experimental methods, but accurate simulation of the complex turbulent flows in the two dimensional configuration is limited by the accuracy of the turbulence models being used. Previous studies on inlet systems have compared CFD results to experiments with reasonable agreement. Welborn et al.[41] provided experimental results for the distortion coefficients in S-shaped ducts, and Zhang et al.[42] used a fine grid to achieve good agreement with the reported values using an algebraic turbulence model. An investigation performed by Smith et al.[33] found good agreement between experimental data and results computed using an algebraic turbulence model. In order to determine the optimum turbulence model for this class of flows, previous work on diffusers will be relied upon. Recent works [22,37] performed sensitivity studies on diffusers using different turbulent models and concluded that either the Spalart-Allmaras (SA, with rotation corrections) or the SST using k-ω two equation model be used. This approach was used previously for the design of a S-duct inlet [33,41].

Figure **38** shows the results on the total pressure recovery (PR) and the flow distortion index (DC60) at several geometric combinations for the S-duct study. Nine optimum diffusers were

selected from the Pareto optimal solution using the coarse grid, and computations were performed to refine the solution using the fine grid for each of these design points. Figure **38** (right) shows the objective function values calculated with the fine grid. While the flow distortion in the baseline subsonic diffuser was a large increase, the one in the modified subsonic diffuser decreased. The pressure recovery in the modified duct was greater than the one in the baseline, but the difference between them was insignificant, suggesting the total pressure in a moderate subsonic diffuser could be similarly recovered. However there was a big difference of the flow distortion.

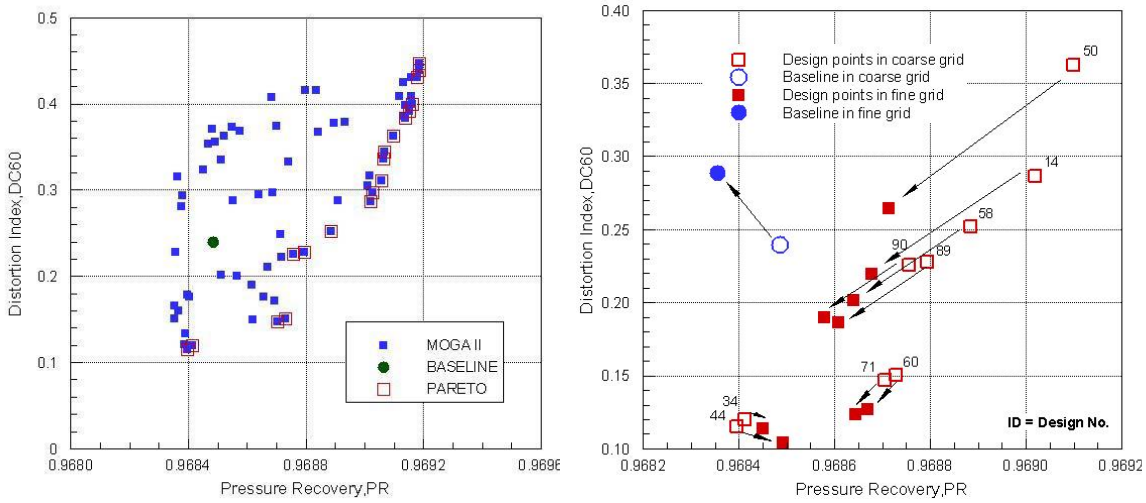

Figure 38: Inlet distortion index and pressure recovery as a function of inlet geometry variations using the coarse grid, and change in results using the fine grid [42].

While these analyses can be a useful tool for S-duct geometries, applicability to the split-wing configuration is limited.

The cross-sectional airfoil shape from Figure 34 was inputted into ICEMCFD using formatted data points. The mesh procedure was scripted, creating numerous meshes for each parameter investigated.

3.6.1 Baseline Mesh and Boundary Conditions

The baseline mesh was based on an H-grid with three O-grids for the top surface, bottom surface and fan nose / motor / motor boat tail. Pressure outlets were chosen for the fan entrance boundaries and pressure inlets were selected for the fan exits, as shown in Figure **39**. In order to account for the mass flow rate ($\dot{m}$) through the fan, all four boundary pressures were altered so that

the sum of the pressure inlets minus the sum of the pressure outlets was equal to zero. The pressure values were altered until the mass flow rate through the fan was within 2.5% of the predicted value. The specific mass flow rates (100% WOT, 80%, 60%, 40%, 20%) came from the fan design tool HAPSS, see Table 4.

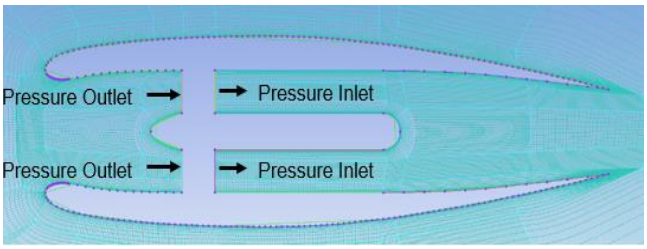

Figure 39: CFD mesh for Baseline model.

The other solid surfaces (upper and lower surfaces, motor, motor boat tail, and fan nose) were idealized as walls with no-slip. The far-field pressure boundary conditions were set 15 chord lengths in all directions. In order to accurately capture the boundary layer laminar – turbulent transitions,

3.6.2 y^+ Estimation

In order to accurately capture the boundary layer and the laminar – turbulent transition, Cole's parameter for boundary layer thickness (y^+) was constrained to less than or equal to 5. Figure 40 shows the y^+ value for each cell in along the outer mold-lines (blue) and inlet mold-lines (red).

While this plot verifies that the boundary layer and transitions can be calculated effectively, the large y^+ values at the leading edge and fan faces suggests that the mesh was only adequate, and could have captured the flow much better with a finer mesh near the no-slip walls.

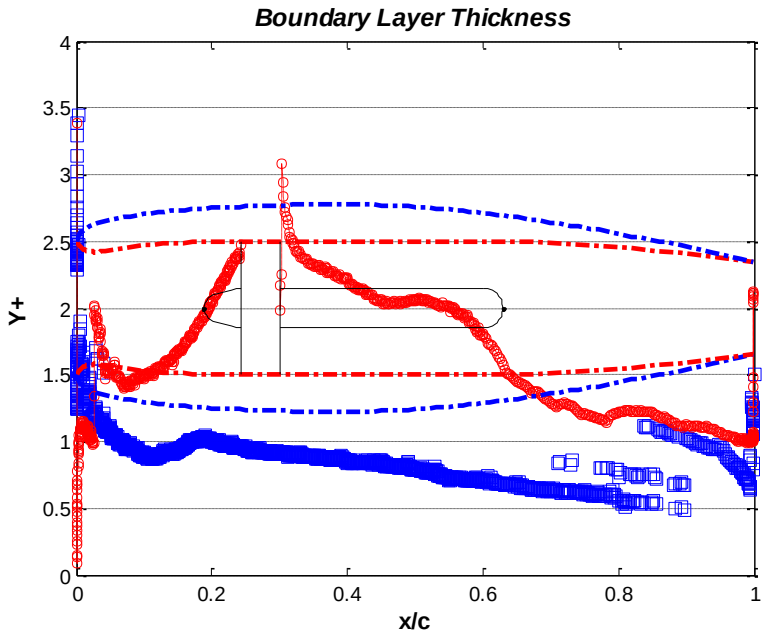

Figure 40: Boundary Layer Thickness (y^+) for baseline case.

3.6.3 Richardson Extrapolation

Richardson Extrapolation is a method of utilize two discrete solutions to systematically refined a mesh. The method can also be used to estimate the exact solution, assuming the rate of convergence is known for the discretization method and mesh refinement scheme [8]. The definition of discretized error for a general solution variable *f* with grid spacing *h* is shown below.

$$\varepsilon_h = f_h - \tilde{f} \qquad \text{(Eq. 3)}$$

f_h is the exact solution to the discrete equations and $\tilde{f}$ is the exact solution to the original partial differential equation. f_h can be expressed in a power series in h as,

$$f_h = \tilde{f} + g_1 h + g_2 h^2 + g_3 h^3 + O(h^4) \qquad \text{(Eq. 4)}$$

where the coefficients *g* are the derivatives of the exact solution to $\tilde{f}$ with respect to the grid size *h*. Therefore,

$$\varepsilon_h = f_h - \tilde{f} = g_1 h + g_2 h^2 + g_3 h^3 + O(h^4) \qquad \text{(Eq. 5)}$$

The Standard Richardson Extrapolation, formulated by Richardson (1911), applies to numerical schemes that are second-order accurate with factor of two increase for decrease in mesh refinement from the original mesh. Therefore, a numerical scheme was chosen that eliminates the g_1 term. For a grid spacing *h* and 2*h*, the following power series would result,

$$f_h = \tilde{f} + g_2 h^2 + g_3 h^3 + O(h^4)$$
$$f_{2h} = \tilde{f} + 4g_2 h^2 + 8g_3 h^3 + O(h^4) \quad \text{(Eq. 6)}$$

Solving for g_2 yields,

$$g_2 = \frac{f_{2h} - f_h}{3h^2} - \frac{7}{3} g_3 h + O(h^2) \quad \text{(Eq. 7)}$$

By substituting equation Eq. 7 into Eq. 6 and eliminating all third-order terms, the Standard Richardson Extrapolation is demonstrated as,

$$\bar{f} = f_h + \frac{1}{3}(f_h - f_{2h}) \quad \text{(Eq. 8)}$$

where $\bar{f}$ is the exact solution. The Richardson Extrapolation can also be applied to error estimation of a discretization scheme. For a second-order scheme, a third or fourth-order exact solution can be approximated as,

$$f_{exact} = \frac{4}{3} f_1 - \frac{1}{3} f_2 \quad \text{(Eq. 8)}$$

where f_1 is the first mesh and f_2 is either twice as fine or twice as coarse. The order is dependent on whether the odd terms in the Taylor Expansion are absent [30]. The actual fractional error A_1 of a fine grid solution can be expressed as,

$$A_1 = \frac{f_1 - f_{exact}}{f_{exact}} \quad \text{(Eq. 9)}$$

These principles were applied to the baseline CFD model for determining the Richardson Extrapolated Solution. All CFD cases (minus the coarse mesh examples) were completed using the same script, so the cell placements and orientations are all the same. The Richardson Extrapolation Solution offset (difference between the 'fine mesh' and 'Richardson Extrapolated Solution') was then applied to the remainder of CFD cases, called 'Discretization Offset'. See Figure 41. The error bars in Figure 41 refer to the difference between the specific mesh value and the value or the Richardson Extrapolated Solution.

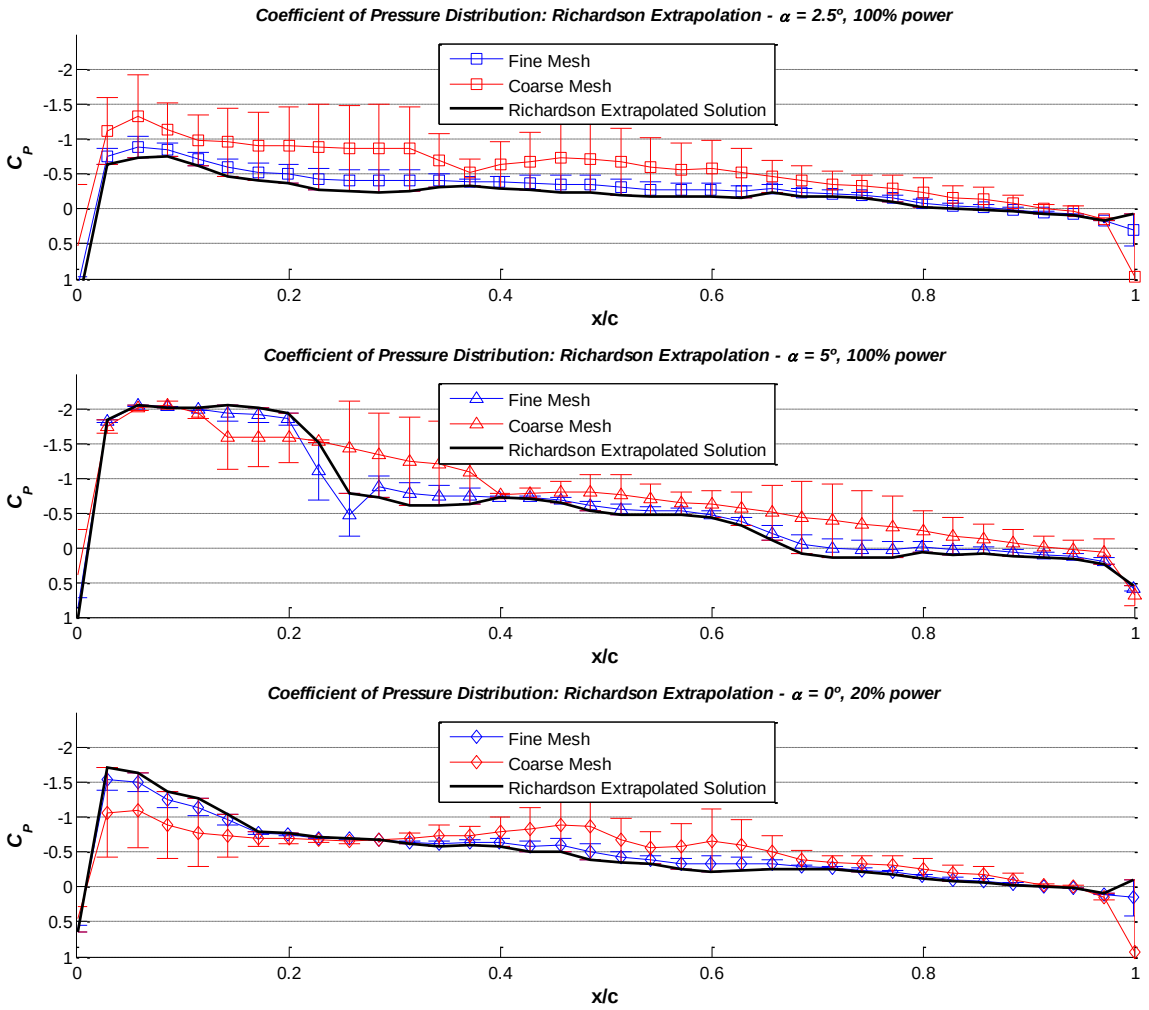

Figure 41: Richardson Extrapolation Cases (M = 0.65 [all]; α = 2.5º, 5º, and 0º [top, middle, and bottom]; ṁ = 55.72 lbm/s, 55.72 lbm/s, 30.64 lbm/s [top, middle, and bottom]).

3.6.4 Verification and Validation of CFD

There are several steps to provide verification and validation of the CFD models. Firstly, the Richardson Extrapolated solution bias was added to each CFD case, based on Mach number, angle of attack, and mass flow rate. Secondly, the difference between the NACA Symmetric Airfoil and the comparative CFD was applied (this can be seen in Case 1). Together, these offsets represent the error bars seen in Figure 42 through Figure 47. The offsets were applied both in additive and subtractive manner, creating a region of confidence around the CFD results.

4. Results

The test cases were broken up into 14 unique comparisons, shown in Table 7. Each comparison case has a specific Mach number (M), angle of attack (∝), and Reynold's Number (Re), with the exception of the ∝ sweep cases. These cases can also be seen in a different format in Inlet Shape Considerations for Split-Wing Electric Distributed Propulsion Tradespace (see Table 6).

Table 7: Comparison cases and results.

Case	Parameter	NACA	CFD
1	C_P M = 0.2 ∝ = 0º Re = 1.80e6	✓	✓
2	C_P M = 0.2 ∝ = 4º Re = 1.80e6	✓	✓
3	C_P M = 0.65 ∝ = 0º Re = 7.43e6	✓	✓
4	C_P M = 0.65 ∝ = 4º Re = 7.43e6	✓	✓
5	C_P M = 0.65 ∝ = 0º Re = 1.93e7		✓
6	∝ M = 0.65 Re = 1.93e7		✓
7	ṁ & toc M = 0.65 ∝ = 0º Re = 1.93e7		✓
8	M & toc M = 0.65 ∝ = 0º Re = 1.93e7		✓ Inlet Only
9	$\bar{A}_{th}$ M = 0.65 ∝ = 0º Re = 1.93e7	✓	✓

Test Cases 1 was run Mach 0.20 and angle of attack of 0º. It had two parts: a direct comparison of the NACA Symmetric Airfoil geometry using CFD and a scaled-down cross-section

of the baseline cross-section depicted in Figure 34. Case 2 moved the geometry from Case 1 (scaled cross-section) to angle of attack of 4º. Case 3 and Case 4 altered the speed of Case 1 to Mach 0.65; Case 3 looked at an angle of attack of 0º and Case 4 was 4º. Test case 5 through 9 looked at the baseline cross-section at cruise conditions (M = 0.65, Re = $1.93*10^7$) for coefficient of pressure (C_P), angle of attack ($\propto$), mass flow rate through the inlet ($\dot{m}$), thickness-to-chord ratio (toc), Mach number (M), and throat area ratio ($\bar{A}_{th}$), respectively. The CFD baseline had a much larger throat area ratio that the CFD representation used in Cases 1, 2, 3, and 4, which is shown in Case 9. The error bar valuation for Cases 1 through 4 is depicted in Section 3.6.4.

For each case, the respective 2-D airfoil geometry was presented on the right of each plot with the title 'Inlet Geometry'. Only the first 30% of the chord was chosen as it adequately demonstrated the difference between results on the left and inlet geometries on the right. CFD cases included the motor / fan geometry, which impacted the leading and trailing edge results. All colors are correlative.

4.1 Case 1 Comparison (M = 0.20 & $\propto$ = 0º)

Case 1 looked at takeoff speed conditions (M = 0.20) for $\propto$ = 0º. This case can be approximated as a takeoff / pre-rotation condition. The upper portion of Figure 42 shows the NACA Wartime Report symmetrical inlet and the corresponding CFD for that geometry and offsets. The lower portion shows the same NACA geometry along with a scaled CFD cross-section of the baseline cross-section with the inlet / fan / motor cross-section.

The purpose of this case was to verify the CFD mesh and turbulence model were accurate enough for the NACA symmetrical geometry as well as identify the difference between the NACA symmetrical geometry and a scaled-down version of the CFD baseline configuration.

The CFD case appears to capture the correct pressure distribution, with the exception of the leading edge for the fan / motor scaled cross-section geometry and the leading. The actual baseline configuration has a much larger throat area ratio, as seen in Figure 55.

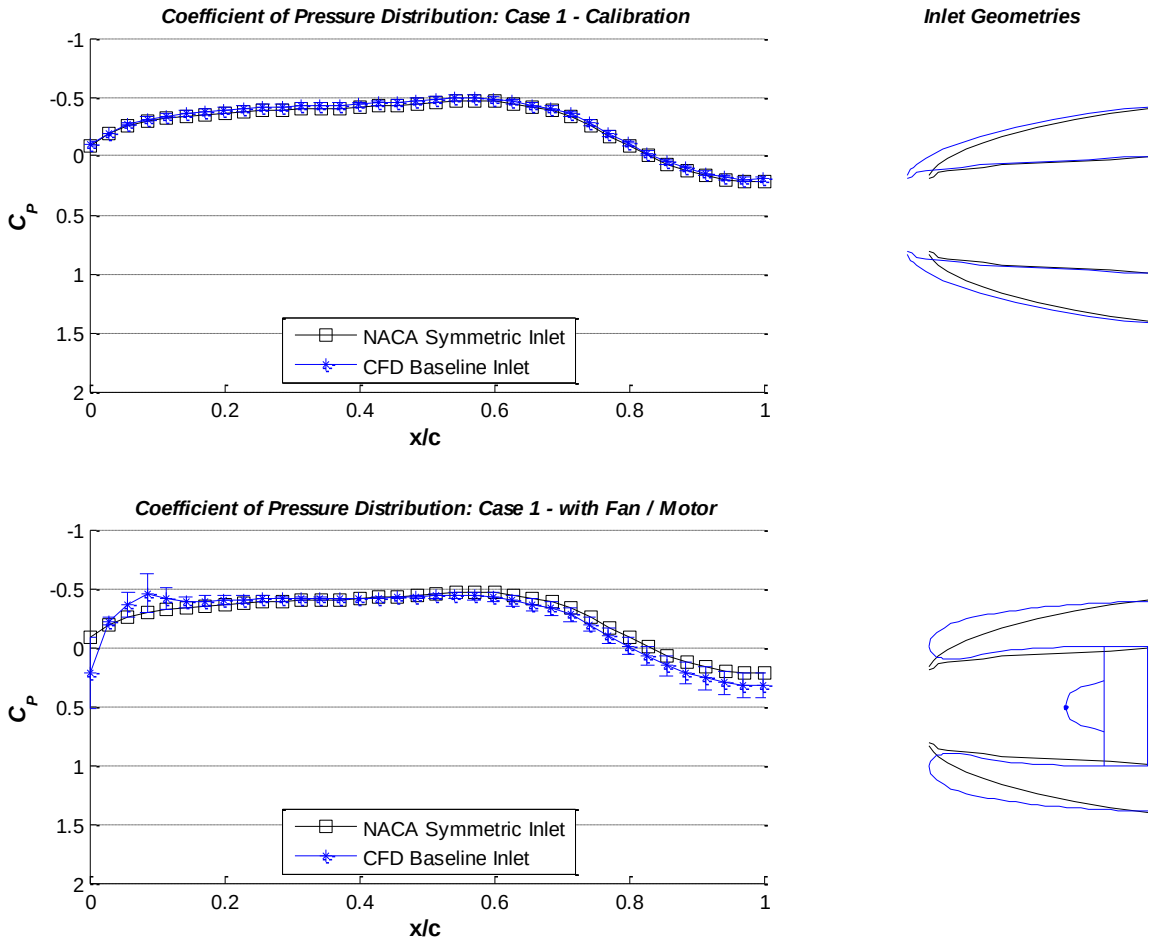

Figure 42: Case 1 Comparison Study, Upper and Lower surfaces equal (M = 0.20, ∝ = 0º, Re = $1.80*10^6$).

4.2 Case 2 Comparison (M = 0.20 & ∝ = 4º)

Case 2 moved the angle of attack (∝) to 4º from Case 1. This case can be compared to a takeoff / rotation condition. For this case, only the first 30% of the chord was captured during the NACA wind tunnel test. Both computational methods matched favorably with the wind tunnel data minus the leading edge (trailing edge not captured in the wind tunnel data).

For ∝ = 4º, the upper and lower surfaces no longer mirrored each other, thus both surfaces were shown as seen in Figure 43.

There was no case for takeoff speed condition with ∝ = 8º because that condition was not investigated during the NACA study, the three α settings (0º, 4º, and 8º) for the CFD model are shown in Figure 44. The streamlines were added to show the flow through the inlet and around

the outer surfaces. The left plots show coefficient of pressure (C_P) and the right plots show Mach number (M).

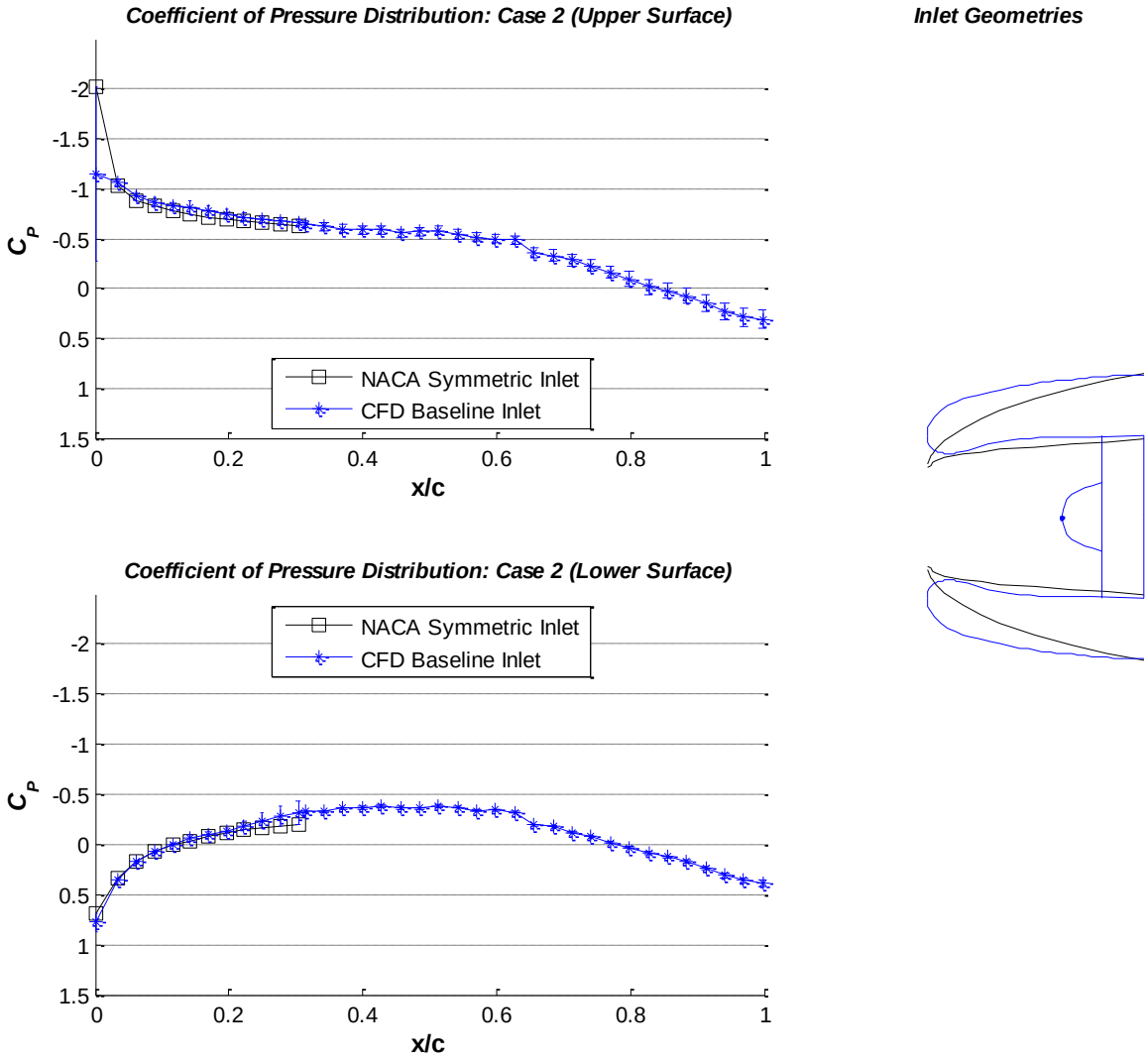

Figure 43: Case 2 Comparison Study (M = 0.20, $\propto$ = 4º, Re = 1.80*10^6).

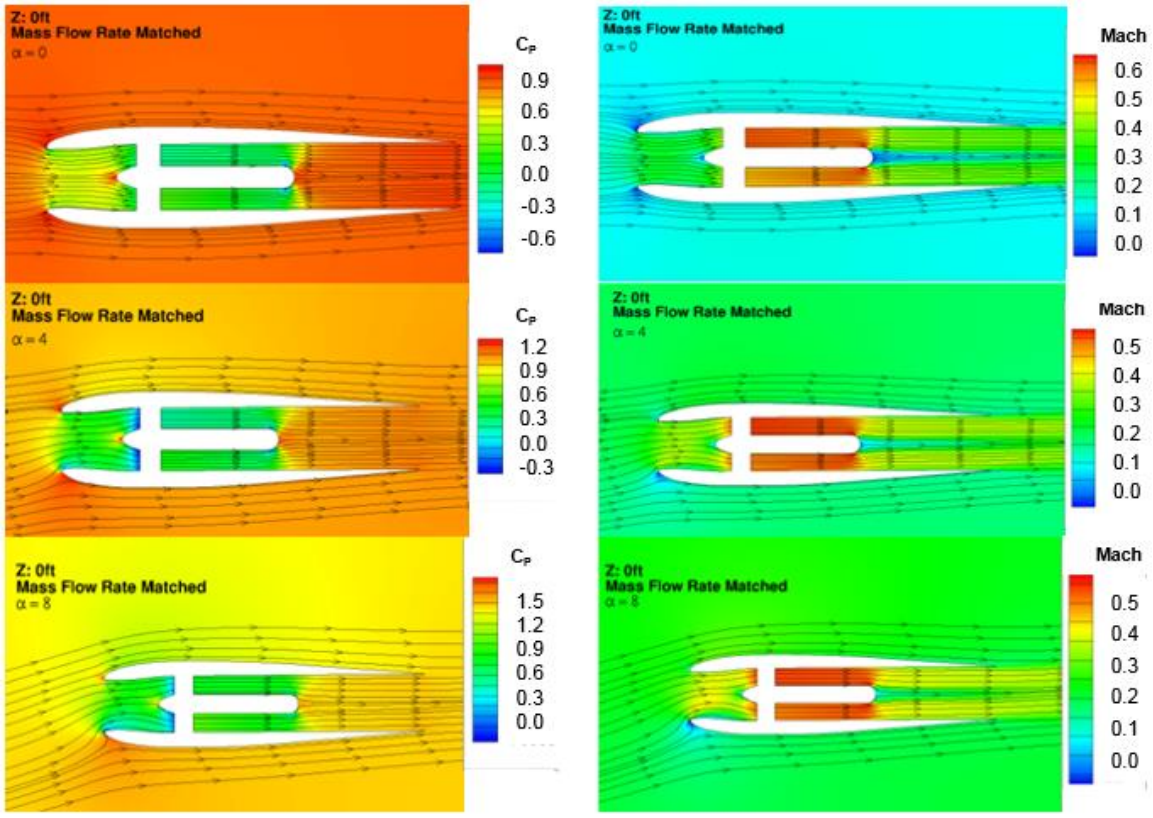

Figure 44: Coefficient of Pressure (L) and Local Mach number (R) CFD Results for takeoff conditions (M = 0.20, Alt = 0kft, $\propto$ = 0º - top, 4º - middle, and 8º - bottom).

4.3 Case 3 Comparison (M = 0.65 & $\propto$ = 0º)

Case 8 compared the NACA Wartime Report symmetrical airfoil and a scaled-down CFD geometry with the motor fan assembly. This case represents cruise conditions for a TeDP B737 / B757 replacement. Similarly to Case 1, this case showed very good agreement between the wind tunnel data and the computational methods, but the computational models diverting from the wind tunnel data at the leading and trailing edges. For the leading edge, the blunt inlet shape of the CFD model accounted for the decreased coefficient of pressure values. For the trailing edge, the mixing flow between the nozzle and the flow above and below the airfoil accounts for the disparity in pressures between the CFD and wind tunnel data.

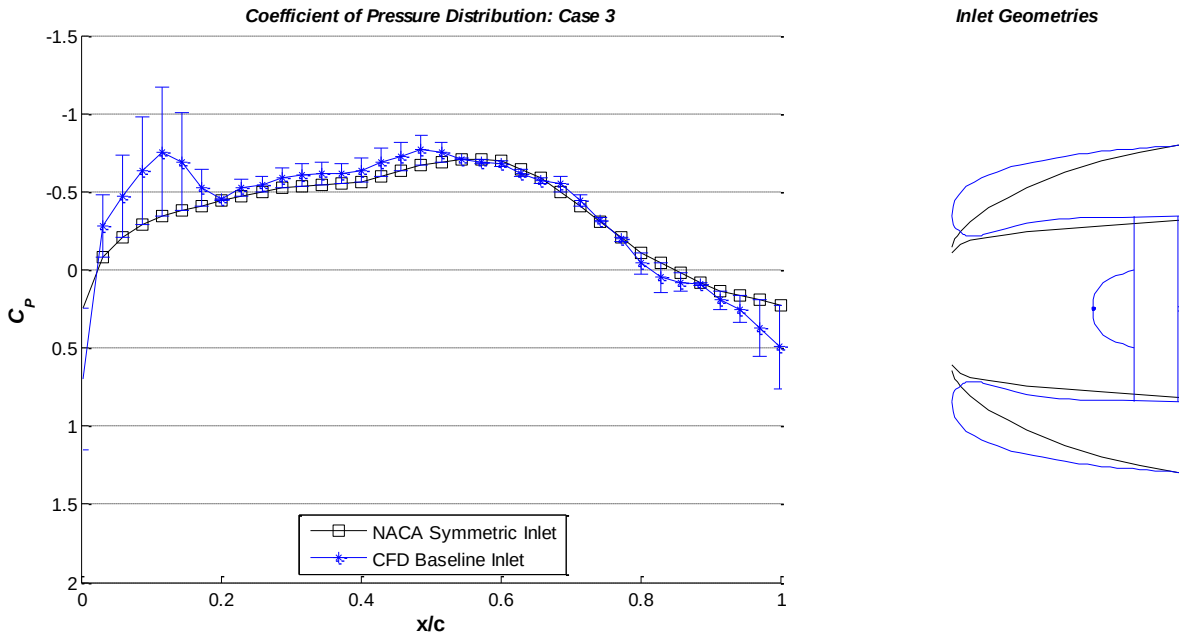

Figure 45: Case 3 Comparison Study, Upper and Lower surfaces equal (M = 0.65, $\propto$ = 0º, Re = $7.43*10^6$).

4.4 Case 4 Comparison (M = 0.65 & $\propto$ = 4º)

Case 4 was the last comparison study, with top-of-climb condition (M = 0.65 and $\propto$ = 4º) modeled. Similarly to Case 2, only the first 30% of the chord was recorded during the NACA study in 1944. Even with the lack of full dataset, both computational methods have good agreement.

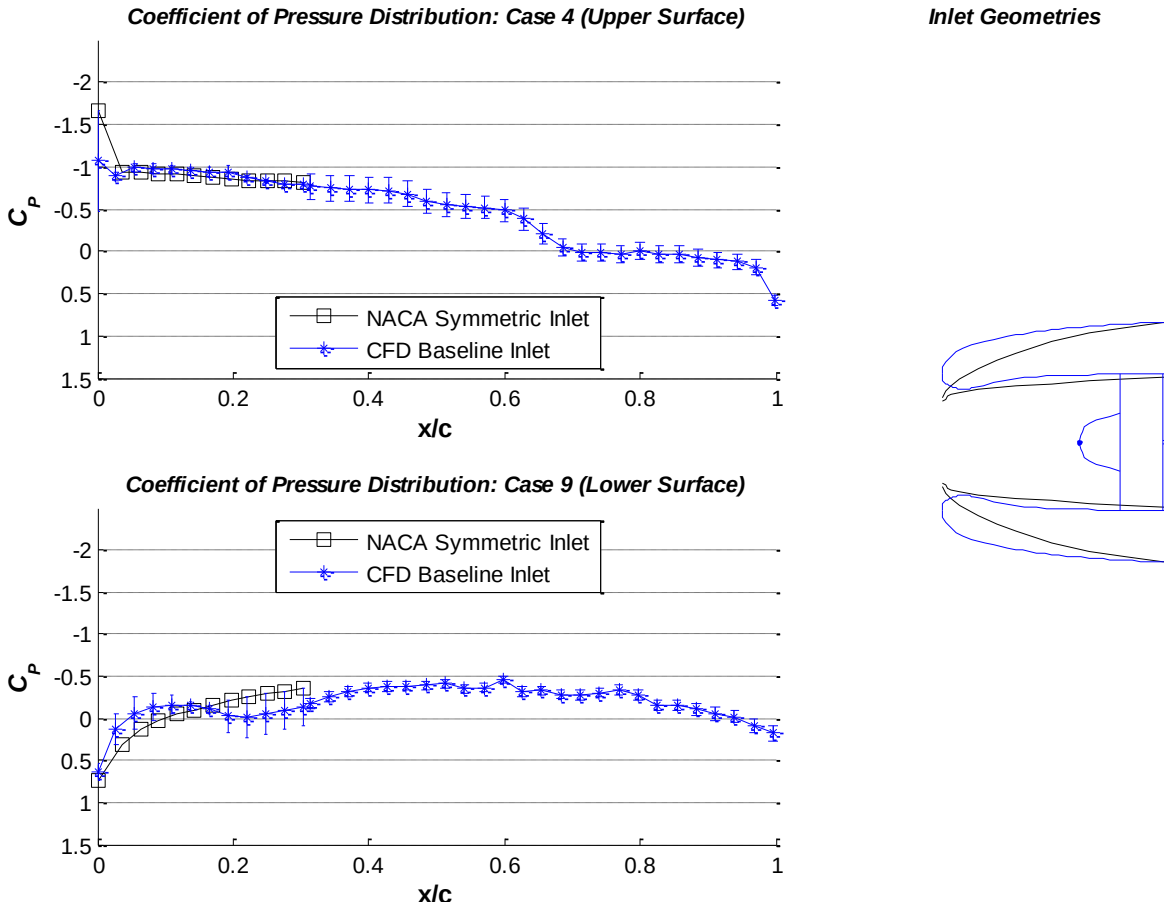

Figure 46: Case 4 Comparison Study (M = 0.65, $\propto$ = 4º, Re = 7.43*10^6).

4.5 Case 5 Study (CFD Baseline, M = 0.65 & $\propto$ = 0º)

Case 5 through Case 9 deal with the CFD baseline and represent the primary thrust of this thesis. The chord for the CFD baseline cross-section derived from the 2010 ESAero SBIR was 127" long with a Reynold's Number of 1.93*10^7. Mach 0.65 was chosen as it matched the NACA wind tunnel data and was between 0.65 and 0.75, which would be feasible for an electric or hybrid-electric regional airliner study. The electrical power demand for high speed cruise necessitates slower cruise speeds until technology can mature.

The CFD method included error bars that relate to Case 8 (M = 0.65, $\propto$ = 0º).

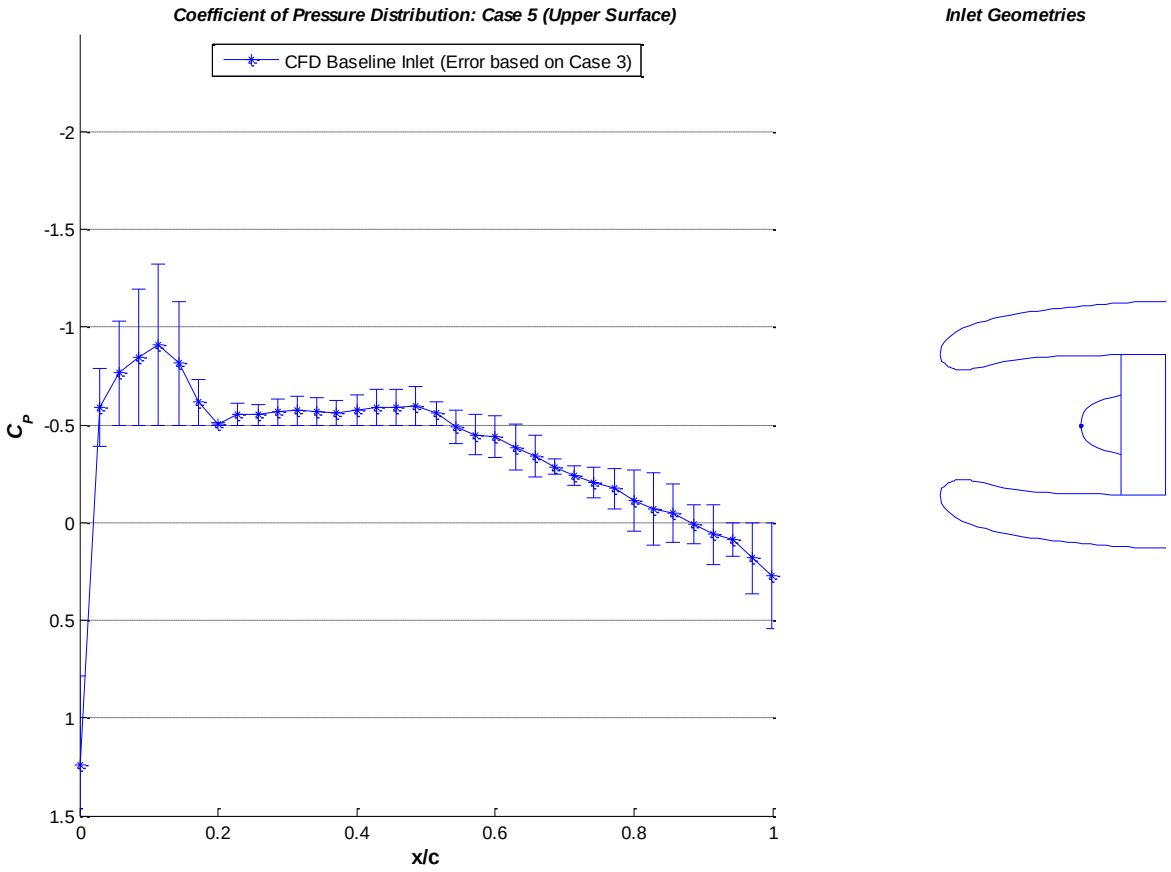

Figure 47: Case 5 Comparison Study (M = 0.65, $\propto$ = 0º, Re = $1.93*10^7$).

Similarly to Case 2 with the $\propto$ sweeps for takeoff conditions, Figure 48 shows a validation method for an $\propto$ sweep at cruise conditions. This comparison shows the analysis for this paper and the preliminary analysis by Dr. Russ Cummings of AFRL as part of a SBIR proposal. Dr. Cummings approximated the fan / motor assembly as complete pressure sinks and sources, without consideration for the fan nose, fan face, and motor, but the exterior aerodynamics were very similar. Both studies had very good agreement with the exception of the inlet flow, which is expected due to the difference in geometries, and flow separation on the upper surface during high angles of attack. The flow into and out of the inlet and nozzle appear very similar between studies.

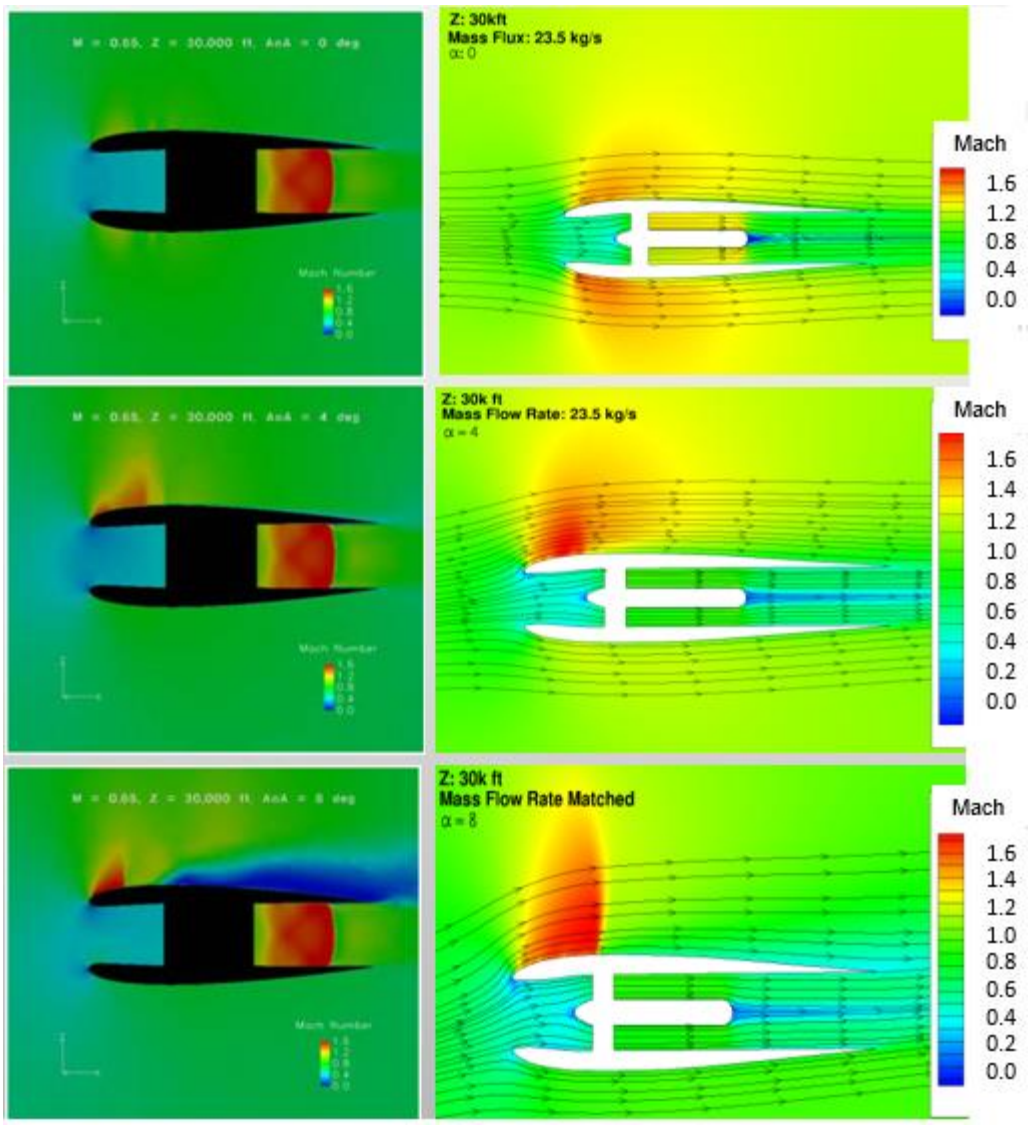

Figure 48: Local Mach number - CFD validation comparison with AFRL study (M = 0.65, Alt = 30kft, $\propto$ = 0º - top, 4º - middle, and 8º - bottom).[11]

4.6 Case 6 Study ($\propto$ Sweep, M = 0.65)

Case 6 performed an $\propto$ sweep for using 0º, 2.5º, 5º, 7.5º, and 10º, with coefficient of pressure being examined, see Figure 49. Both upper and lower surfaces are shown, with perceptible relationships between $\propto$ and C_P. Both 'Discretization Offset' and difference between wind tunnel data CFD were included, but in this case, the error bars were omitted for clarity.

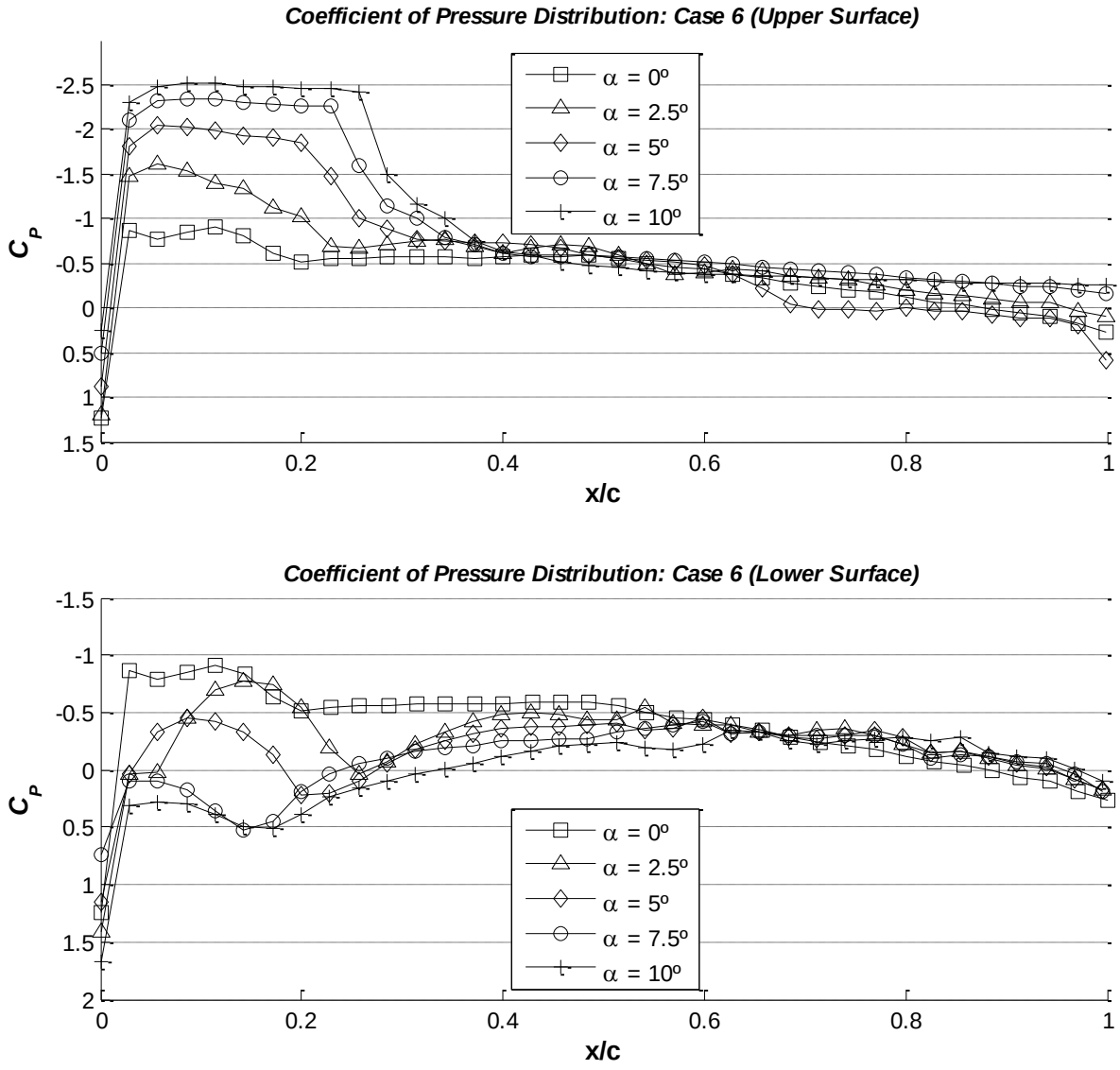

Figure 49: Case 6 CFD sweep for thickness-to-chord ratio of 0.11 (M = 0.65, Re = $1.93*10^7$).

Figure 50 shows the associated coefficient of pressure contours from Figure 48. Similarly to Section 4.6, both Dr. Russ Cummings Phase II SBIR proposal and this study strongly agreed.

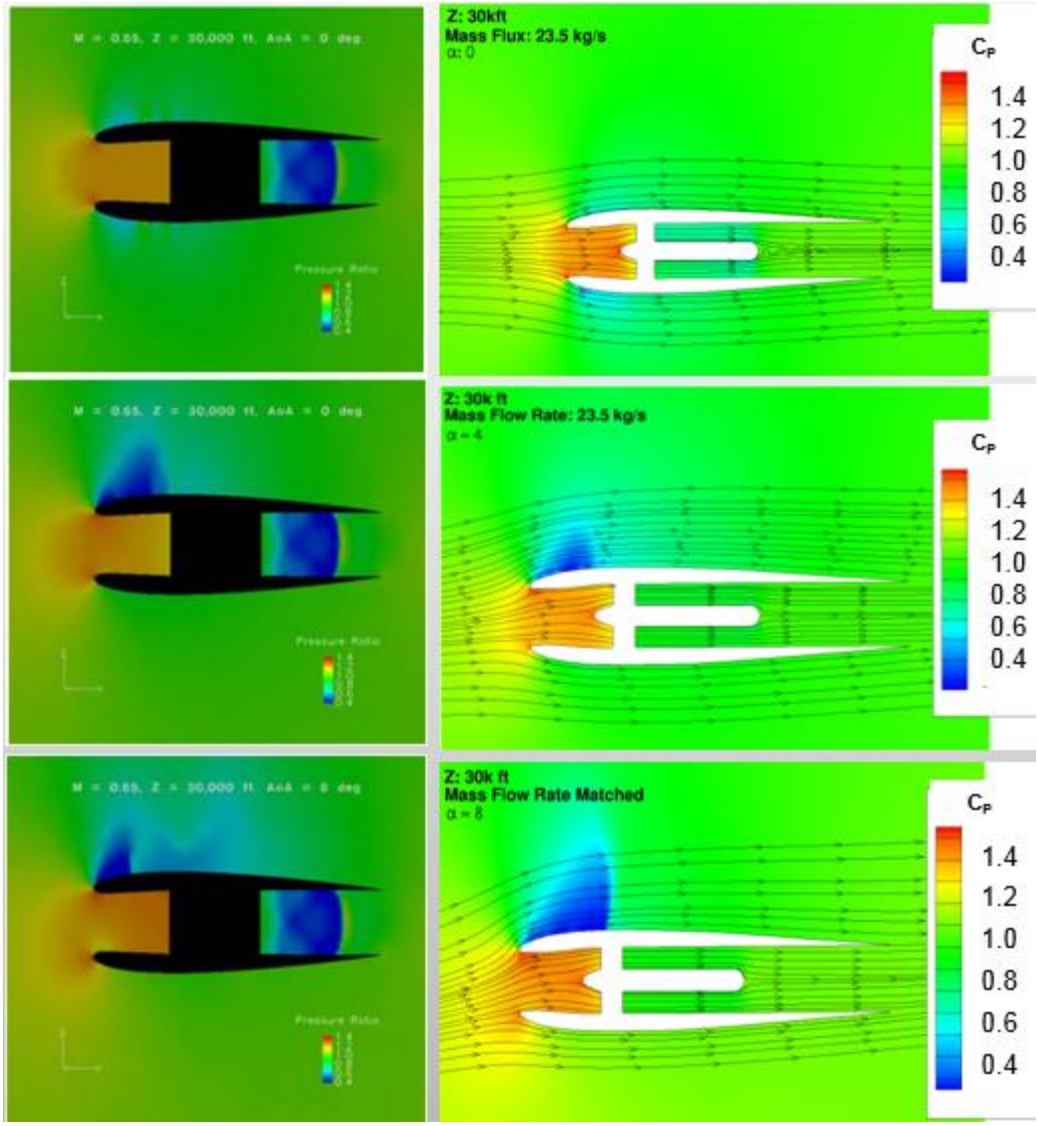

Figure 50: Coefficient of Pressure - CFD validation comparison with AFRL study (M = 0.65, Alt = 30kft, $\propto$ = 0º - top, 4º - middle, and 8º - bottom).[11]

4.7 Case 7 Study (Mass Flow through Fan, M = 0.65 & $\propto$ = 0º)

For Case 7, the Case 5 condition was considered with mass flow rate ($\dot{m}$) as determined by motor power setting, i.e. 'Throttle' and thickness-to-chord ratio (toc) as measured by equivalent airfoil thickness. The blue lines signify the baseline CFD model (11% toc), the red lines designate a toc value of 9% and the green line represents a 13% toc. The upper surface is shown in Figure 51 and the lower surface in Figure 52.

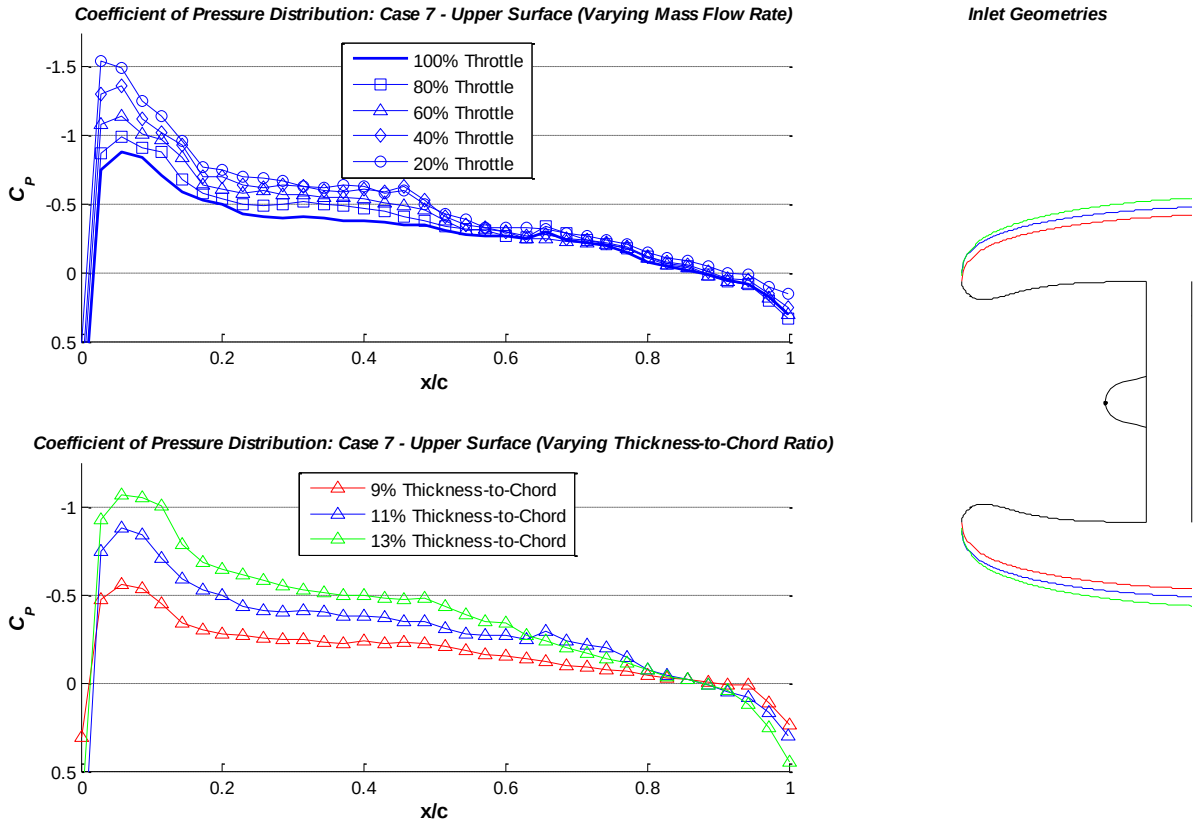

Figure 51: Case 7 (Upper Surface) Coefficient of Pressure distribution for varying mass flow rates (ṁ) and thickness-to-chord ratios (toc) (M = 0.65, $\propto$ = 4º, Re = $1.93*10^7$).

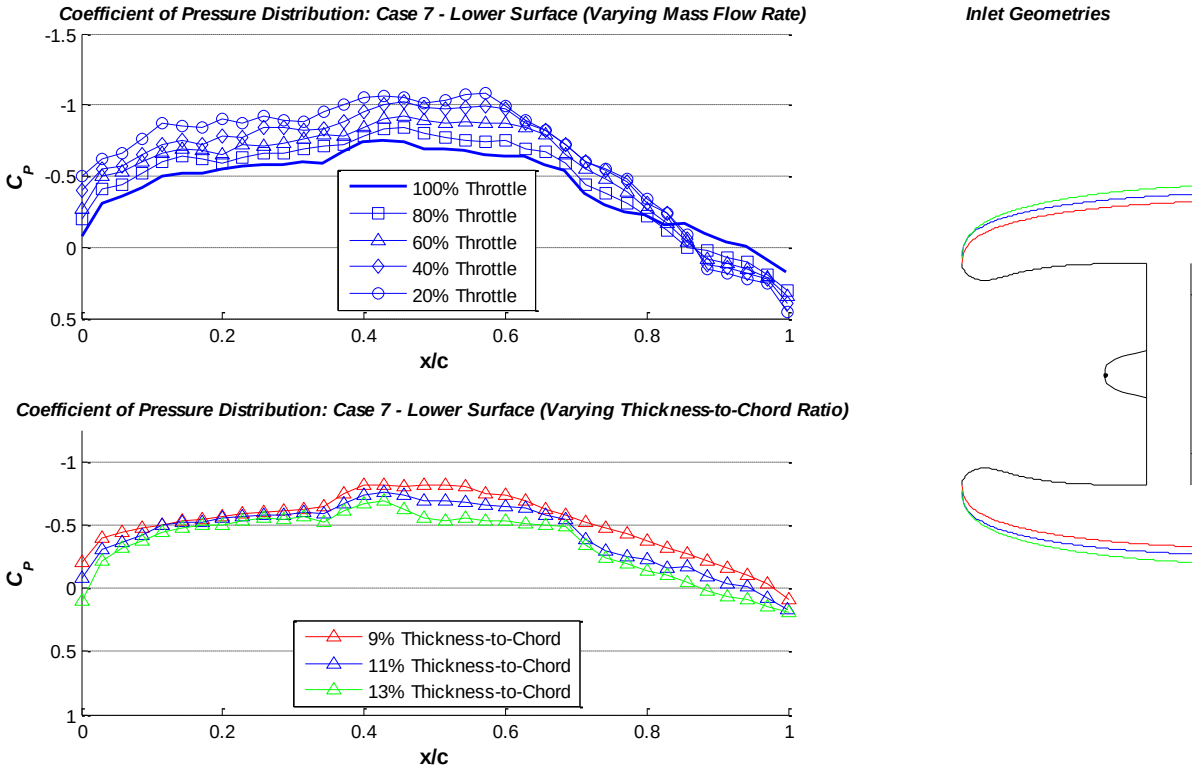

Figure 52: Case 7 (Lower Surface) Coefficient of Pressure distribution for varying mass flow rates (ṁ) and thickness-to-chord ratios (toc) (M = 0.65, ∝ = 4º, Re = $1.93*10^7$).

4.8 Case 8 Study (Inlet Mach Number, M = 0.65)

Varying Mach numbers in the inlet (0% – 30% chord) was considered for Case 8. Fan design tools are better equipped to handle the mass flow rate through a fan, such as HAPSS, which determined the baseline flow used in this study. Local Mach number for differing flight conditions showed perceptible design relationships for pressure changes with α and toc. The upper and lower surfaces are shown in Figure 53 and Figure 54, respectively.

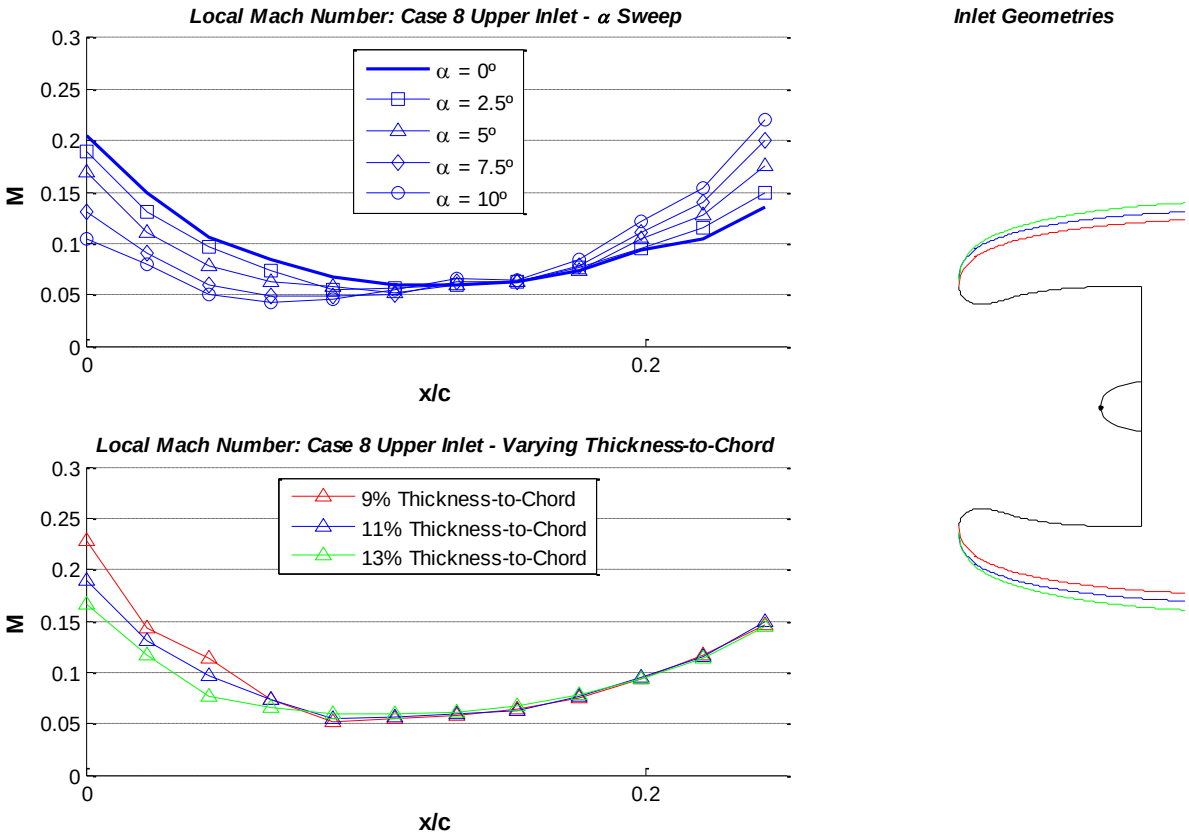

Figure 53: Case 8 (Upper Inlet) Local Mach number for varying mass flow rates (ṁ) and thickness-to-chord ratios (toc) (M = 0.65, ∝ = 0º, Re = $1.93*10^7$).

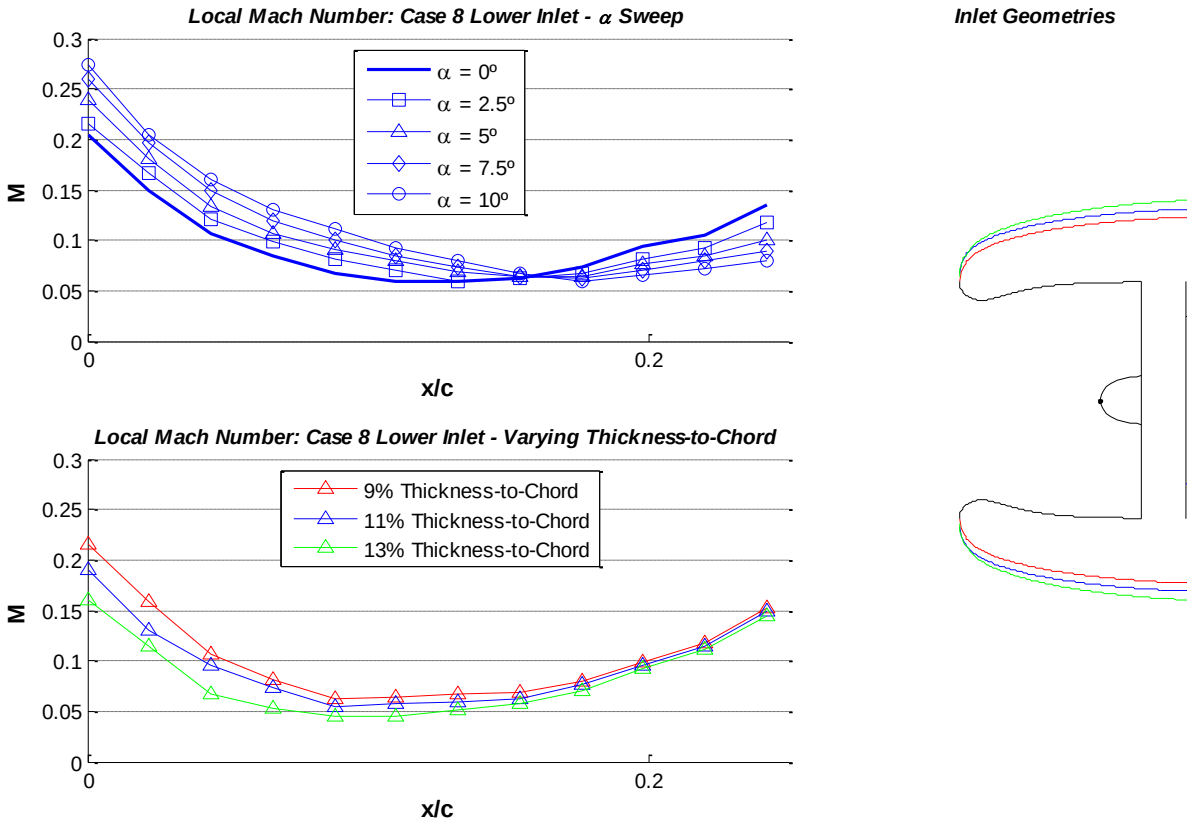

Figure 54: Case 8 (Lower Inlet) Local Mach number for varying mass flow rates (ṁ) and thickness-to-chord ratios (toc) (M = 0.65, ∝ = 0º, Re = 1.80*10^6 – 2.02*10^6).

4.9 Case 9 Study (Throat Area Ratio, M = 0.20 & ∝ = 0º)

Case 9 looked at all datasets for takeoff conditions (M = 0.2, ∝ = 0º); this was the only dataset that includes both NACA wind tunnel datasets and the CFD baseline. See Figure 55. As noted on the right, the inlet sizes are much larger for the CFD baseline study. The CFD baseline throat area ratio difference was responsible for the suction at the leading edge. The dotted black line shows the fan / motor assembly for the CFD cases. Every other line is associated with the C_P distribution on the right.

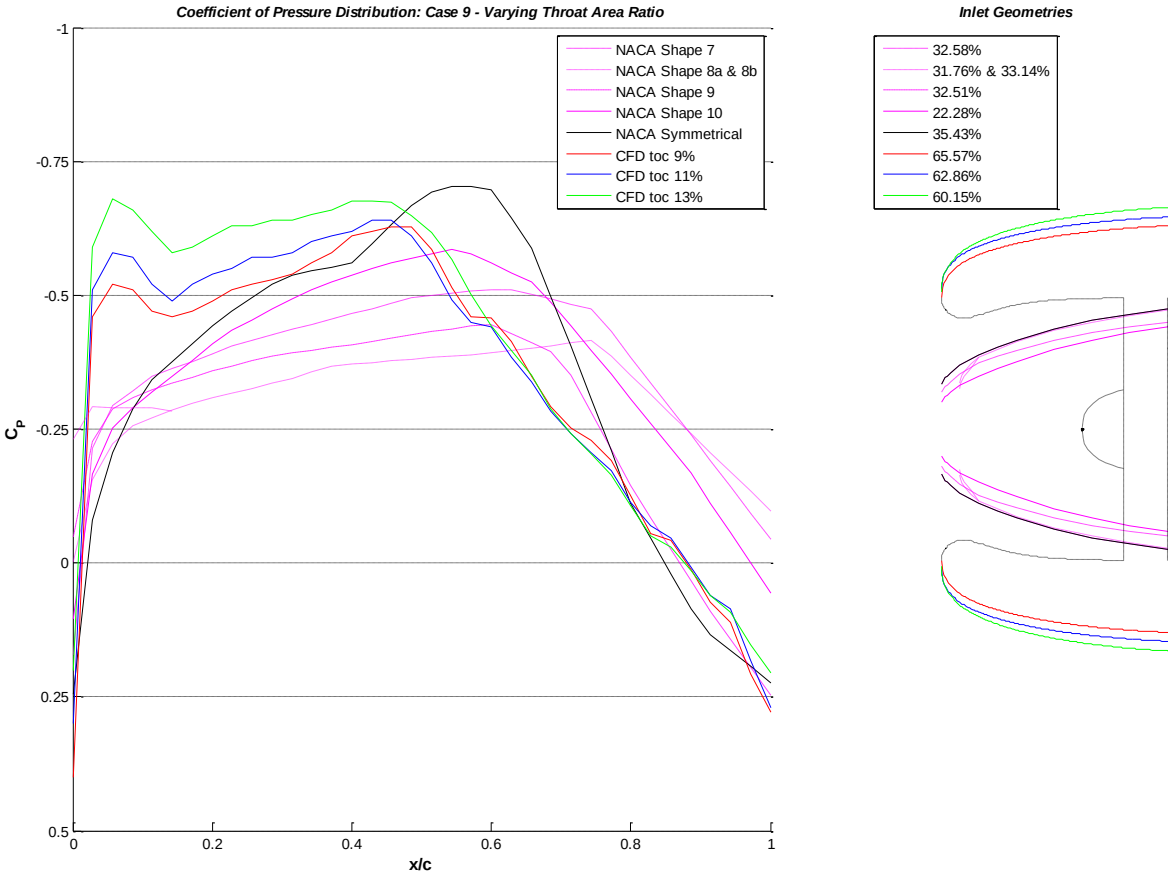

Figure 55: Case 9 Coefficient of Pressure distribution for varying throat area ratios (M = 0.2, $\propto$ = 0º, Re = $1.80*10^6$ to $2.02*10^6$).

5. Conclusions

5.1 Discussion of Performance Metrics

This study focused on several performance metrics for an inlet of a split-wing configuration, specifically Mach number (M), angle of attack ($\propto$), mass flow rate ($\dot{m}$), and throat area ratio ($\bar{A}_{th}$). These parameters are shown in Figure 42 though Figure 55.

The speed of the flow (M) around the outer mold lines was disrupted due to the leading edge lip. As shown in Figure 48, the flow around the cross-section was accelerated due to the bulbous leading edge lip. This could potentially cause shocks near the leading edge, significantly reducing the effectiveness of this cross-section to produce lift and limit drag. The flow going into the inlet had to be decelerated to handle to mass flow rate requirements for the fan model.

The inlet diffuser maintained decent pressure recovery for baseline conditions (full power), but adverse pressure recovery conditions existed for partial power settings (see Figure 53 and Figure 54),

Overall, the Mach number evaluation concluded with partial acceptability for differing flight conditions, however, lip radius and inlet contouring were demonstrated as primary design drivers in order to maintain usefulness.

For varying angles of attack ($\propto$), the split-wing cross section demonstrated comparable results from the baseline inlet design from the NACA Wartime study, with similar shock points for high $\propto$ conditions, as seen in Figure 49 and Figure 50. There were some pressure losses inside the lower lip of the inlet at high $\propto$ that would cause undue cyclic loading on the fans.

Throat area ratio ($\bar{A}_{th}$) was a driving parameter for leading edge pressure spikes. As seen in Figure 55, increased inlet area significantly increased the pressure over the outer mold lines. The remainder of the airfoil demonstrated adequate pressure recovery, but ultimately, sizing the fans (and therefore inlet area) to be as small as possible would be most advantageous.

5.2 Observed Benefits and Drawbacks of the Split-Wing Configuration

Ultimately, there was insufficient evidence to support the claim that split-wing design would be an aerodynamic competitor to over-wing or under-wing configurations. The pressure spike due

to the increased frontal area of the split-wing was significant, and no apparent pressure profile benefits were demonstrated in this study.

The split-wing design presents multiple exciting opportunities, especially for tightly coupled aerodynamic and propulsion system control, while also reducing noise and emissions. While the aerodynamic benefits were unsubstantiated in this study, further investigation would have to be conducted in order to fully rule out this configuration.

This study does demonstrate some good rules-of-thumb for future designers: first, the inlet area significantly degrades the inlet aerodynamic performance, suggesting that smaller inlets / smaller fans are more desirable. This means that long narrow motors would be necessary, which could levee a weight penalty on the design. Additionally, inlet contouring would be necessary in order to fully capture the rectangular to circular geometries present in the diffuser and nozzle. These shape optimizations could dramatically improve pressure recover and lead to an attractive alternative to the over-wing and under-wing configurations.

5.3 Model Assumptions

There were several assumptions made in order to pare down the complexity of the problem, including:

- Assumed no adverse normal forces, including starving of adjacent fans were present along the inboard wing section.
- Assumed no rotational physics for the actual fan, fan was idealized as pressure inlet and outlet boundary conditions.
- All required power electronics, cabling, and internal structure necessary to power and house the electric motors were omitted in the 2-D cross-section. These systems would have to be integrated in a more in-depth point design.
- The fan cowling was assumed to carry the load. Additional rib sections would be necessary between fan assemblies to maintain wing rigidity.
- The motor sizing methodology assumed linear technology scaling, which is optimistic.

- Nozzle design was not considered, which would provide significantly improved thrust potential for the model. Direct fan / motor performance was outside the scope of this study.

The first assumption, no adverse normal forces present, was made in order to approximate the flow through the duct with a 2-D representation. The split-wing design will inherently have complicated flow patterns as these high power ducted fans are placed in close proximity.

The Rolling Hills study, discussed in Section 2.3 investigated the flow relationships for closely spaced ducted fans. Their findings suggested that the ducted fans would scavenge each other's incoming flow, potentially reducing the overall effectiveness of the design. There were some other interesting outcomes as well, including sharp increase in fan dynamic pressure (q) when a neighboring fan was shut off, providing increased thrust. While the Rolling Hills study was also preliminary, this relationship could be leveraged as a method of reducing tail size. In aircraft design, the tail size is primarily driven by the need for controllability during 'one engine inoperable' (OEI) takeoff conditions. For ducted fans, and specifically the split-wing design, one fan inoperable (OFI) would be more apropos for tail design. The thrust increase due to increased q resulting from an OFI condition could effectively compensate the loss of thrust from the lost fan, reducing the negative yaw moment incurred, and therefore potentially reducing the size of the tail.

No rotational physics were considered in the CFD analyses, as it would be very computationally expensive and the added accuracy and precision would only marginally improve these analyses. After all, the focus of this thesis was not to develop an appropriate fan / motor performance and design tool, as that capability already exists in other works, including HAPSS[16]. All flow predictions near the fan face and exit should be highly scrutinized, as significant turbulent flow and vorticity would be present due to the close proximity of the inlet mold-lines and fan tips.

The electric system architecture necessary for realizing an electric or hybrid-electric distributed propulsion system would be significant and design specific. All cables, cooling lines, fuel lines (if turbo-generators were located in the wing), as well as structural considerations would have to be designed, and their inclusion into the design would dramatically distort the inlet flow aft

of the fan. The flow on the upper and lower surfaces and inlet / diffuser would be only be marginally affected. These complexities would only dilute and complicate the study.

The split-wing cross-section presented in this thesis did not account for load-bearing members between the upper and lower surfaces of the inlet. The fan cowling, shown in Figure 34 with the dotted lines differentiating the flow into and out of the fan was assumed to carry structural load, as well as rib sections which are not present in this study. These rib sections would be spaced in between each fan / motor assembly as shown in Figure 6 and Figure 13.

The electric motor in this study was based on the Remy International HVH-250-115-POC3 electric motor. The motor was scaled with the diameter squared and was proportional to length, as shown in Eq. 2. Motor sizing is design specific, allowing significant flexibility in motor design, and with the electrical and thermal demands for an 800 hp motor suggested in this study, scaling the motor as crudely as suggested in Eq. 2 is probably inadequate. However, the power-to-weight suggested for the scaled Remy motor agrees well with hybridization studies conducted at NASA, Boeing, General Atomics, and others [3,8,27].

Nozzle design fell outside the scope of this work, but the flow through the system and resultant forces are largely dependent on the nozzle design. Fan / motor performance fell outside the scope of this work as well. The split-wing configuration would be a favorable configuration for morphing nozzles and thrust vectoring. These concepts would need to be considered for a more rigorous point design.

5.4 Lessons Learned

This inlet design tool produced several lessons learned for future work considerations, including:

- A symmetric airfoil was used to reduce project complexity and provide more identifiable relationships for α, toc, $\dot{m}$, and $\bar{A}_{th}$. A cambered airfoil would be recommend for a TeDP B737 replacement design.
- The CFD representation of the 2-D cross-section for the split-wing design adequately captured the flow physics through the inlet.

- The CFD results did not account for flow behavior due to neighboring fan / motor assemblies, which is inherent in the split-wing design. These results appeared to be significant enough for further investigation, per the Rolling Hills study in Section 2.3.
- Varying gauge pressure for the pressure inlet / outlet boundaries in the CFD model was an effective method for attaining the desired mass flow rate ($\dot{m}$) for a given flight condition.
- No apparent difference was observed between one equation and two equation turbulence models suggesting Spalart-Allmaras would be preferable due to reduced computational times.

A symmetric airfoil baseline was a preferred method for identifying parameter relationships, but for a more rigorous point design, an airfoil designed for high-subsonic cruise which still provided adequate lift at takeoff would be strongly recommended.

For a rudimentary study, the CFD methodology for capturing flow through the split-wing was adequate, but had several drawbacks, specifically with the rotational physics and inherent 3-dimensionality of the split-wing configuration. The flow leading up to the fan face had favorable agreement with the 2011 SBIR Phase II proposal, as did the flow aft of the motor boat tail through the nozzle.

Also notable in the predictions was the presence of a normal shock in the engine nozzle, seen in Figure 44, Figure 48, and Figure 50. This was caused by the high exit Mach number from the fan / motor flowing into a constant area nozzle. Since the predictions were viscous, boundary layer growth led to flow acceleration up to supersonic Mach numbers and the development of the shock. The shock could be prevented by contouring the nozzle for the designed flow conditions (i.e. morphing nozzle).

5.5 Suggestions for Future Work

This study has revealed several avenues for future work considerations, including:

- Utilizing a medium-cambered airfoil with C_L designed for M = 0.65 to 0.75.

- Performing a 3-D CFD analysis to determine flow behavior for fans in close proximity, similar to the Rolling Hills study in Section 2.3, but for the split-wing configuration.
- Instrumenting an experimental setup with an extruded split-wing cross-section with fan / motor assembly in a wind / water tunnel.
- Accounting for the necessary electric / hybrid-electric system hardware inside the split-wing (i.e. speed controllers, inverters, power cables, power buses, rib sections, cooling lines, and potentially fuel lines).
- Accounting for heat build-up and dissipation generated from the motors, speed controllers, cables, and buses.
- As with all new electric / hybrid-electric configurations, developing a full split-wing aircraft parameterization to account for added weights and locations of propulsive devises, improvements to field performance, tail sizing, and controllability, and considerations for system redundancy and mitigation strategies.

This study utilized a symmetric airfoil, derived from a NACA 0012 airfoil. While a symmetric airfoil allowed for improved characterization for α, $\dot{m}$, toc, and $\bar{A}_{th}$, a symmetric airfoil would probably not be selected for use in an actual electric / hybrid-electric configuration. Depending on the powered lift considerations, the wing either would be designed for cruise efficiency or takeoff / climb performance. Either option would lead to a cambered airfoil, similar to the supercritical airfoil split-wing cross-section shown in Figure 56.

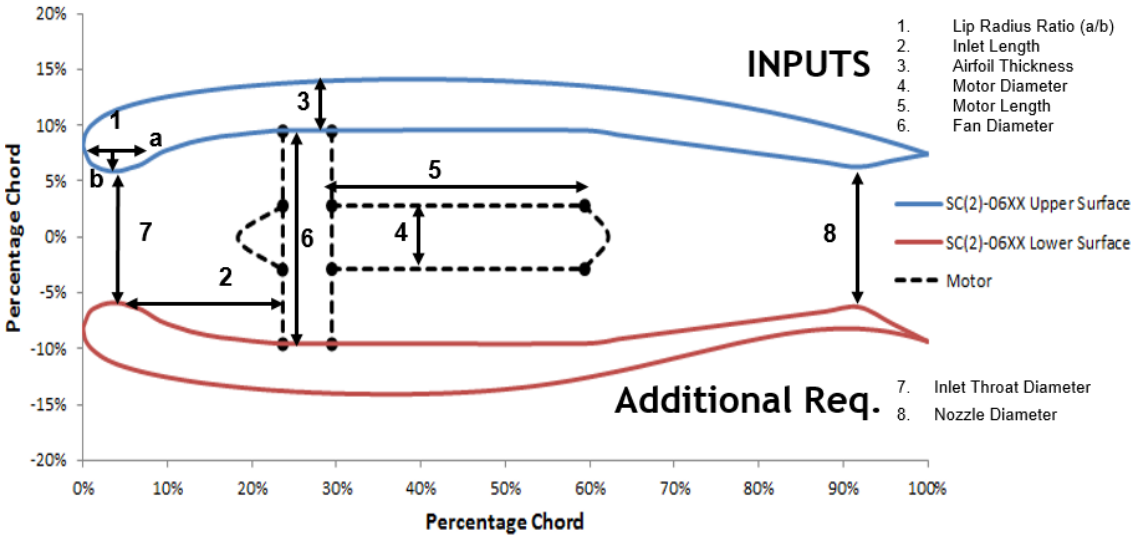

Figure 56: SC(2)-06XX rubberized supercritical airfoil with motor and fan included.

The supercritical airfoil SC(2)-0612 was manipulated in much the same way as the NACA 0012 airfoil shown in Figure 34. The 'XX' term in the caption refers to multiple airfoil thicknesses provided by the tool developed for this study which rubberized airfoil cross-sections. More parameters to be characterized are shown in Figure 56 as well.

3-D CFD analysis would provide insight into several aspects of the design which are not possible with a 2-D analysis, including how the rectangular diffusers behave transitioning into circular fan faces, how ducted fans in close proximity starve each other, and how rotating flow from one fan affects its neighbors. Some of these trends can be surmised from the Rolling Hills study and other studies regarding ducted fans, but the unique split-wing inlet / diffuser / nozzle sections would be novel research.

In order to fully capture the flow through the 3-D split-wing, an instrumented test article would have to be created, and the computational methods could then be validated against the experimental data. Pressure taps throughout the inlet, diffuser, nozzle, and upper and lower surfaces would need to be rigged up. This would signify and major effort however.

Additional electric / hybrid-electric design considerations could also be implemented, providing a more realistic inboard cross-section. Specific items of interest would be wing rib structure to support the fan / motor assembly, power cabling, insulation, power bus architecture, step-up and step-down converters, speed controllers, inverters and other power electronic items.

Each power electronic item would have its own heat sink or cooling method, including but not limited to a fully integrated liquid cooling system. This level of complexity would be necessary for more robust point design, but presents myriad of other design parameters and added complications.

Ultimately, a tool that is modular in nature but that can account for cooling, EMI issues, fan / motor design parameters, and inlet / diffuser / nozzle considerations would accomplish all these future work considerations. Several small business are attempting to develop similar architecture tools, but not specifically for the split-wing configuration.

REFERENCES

1. Advanced Concept Studies for Subsonic and Supersonic Commercial Transport Entering Service in 2030-35 Period. NASA Research Announcement, Washington DC: Pre-Proposal Conference November 29th 2007.
2. Aranake, A., Lee, J.G., Knight, D., Cummings, R.M., Cox, J.L., Paul, M.P., and Byerley, A.R., "*Automated Design Optimization of a 3D Subsonic Diffuser*," submitted to the Journal of Propulsion and Power.
3. Boeing Commercial Airplanes. "*Current Market Outlook 2011-2030".* Seattle, WA :
4. Boeing Market Analysis, 2011.
5. Borer, N., "*LEAPTech Distributed Electric Propulsion Demonstrator*." NASA Langely, © 2014.
6. Bradley, M.K., Droney, C.K., "*Subsonic Ultra Green Aircraft Research – Phase II*," Annual Interim Report #2, Boeing Research and Technology, NASA contract NNL08AA16B – NNL11AA00T, pg. 199 – 324, © Jan. 2013.
7. Crosthwait et al. "*Preliminary Design Methodology for Air-Induction Systems*," SEG-TR-67-1, © 1967.
8. Cummings, R.M., Cox, J.L., Paul, M.P., Byerley, A.R., Decker, R.K., Lee, J.G., Aranake, A., and Knight, D.D, "*Integrated Optimization Study of a Subsonic Diffuser with Offset in Two Planes*," 4th Symposium on Integrating CFD and Experiments in Aerodynamics, von Karman Institute, Rhode-Saint-Genèse, Belgium, Sept. 2009.
9. Del Rosario, R., Koudelka, J., Wahls, R., Madavan N. "*NASA Subsonic Fixed Wing Project Overview",* Cleveland OH: NASA Fundamental Aeronautics Program, 2012 Technical Conference, 2012.
10. Drela, M., Youngren, H., "*XFOIL 6.9."* Last Updated Nov. 2001.
11. Empirical Systems Aerospace, Inc., "*Physics-Based Radiator Design, Sizing & Weight Estimation Tool for Conceptual Design of More-, Hybrid-, and All-Electric Next Gen Aircraft*," Phase I Mid-Term for SBIR contract NNX14CC57P, © 2014.
12. Empirical Systems Aerospace, LLC., "*The Design and Integration of a Distributed Fan Propulsion System within a Split-Wing",* Prepared for Kim, H. D., NASA, SBIR Contract NNX10CC81P, July 2010.
13. Forsythe, J.R., Strang, W., Hoffmann, K.A., "*Validation of Several Reynolds-Averaged Turbulence Models in a 3D Unstructured Grid Code*," AIAA Paper 2000-2552, June 2000.
14. Gibson, A. R., Hall, D., Waters, M., Schiltgen, B., Foster, T., Papathakis, K., "*Superconducting Electric Distributed Propulsion Structural Integration and Design in a Split-Wing Regional Airliner",* AIAA 2011-223-736 : 49th AIAA Aerospace Science Meeting including the New Horizons Forum and Aerospace Exposition, Orlando, FL, 2011.
15. Goldschmied, F. R., *On the Aerodynamic Optimization of Mini-RPV and Small GA Aircraft.* AIAA 1984-2163-960 : 2nd applied Aerodynamics Conference, Seattle, WA, 1984.

16. Goldschmied, F., *Wind Tunnel Test of the Modified Goldschmied Model with Propulsion and Empennage: Analysis of Test Results.* FRG-82-1: David W. Taylor Naval Ship R&D Center, 1982.
17. Green, M. W., *HAPSS, Hybrid Aircraft Propulsion System Synthesis.* Master's Thesis: California Polytechnic State University, San Luis Obispo, 2012.
18. Grismer, M.J., Strang, W.Z., Tomaro, R.F., and Witzemman, F.C., "*Cobalt: A Parallel, Implicit, Unstructured Euler/Navier-Stokes Solver*," Advances in Engineering Software, Vol. 29, No. 3-6, 1998, pp. 365-373.
19. Iannotta B., "*The Power of Electricity*," Engineering Notebook, AIAA, © Oct. 2014.
20. Joby Motors, http://www.jobymotors.com/, accessed 11 August 2014.
21. Kerho, M., Kramer, B., "*Turboelectric Distributed Propulsion Test Bed Aircraft*," NASA ARMD FY12 LEARN Phase I Technical Seminar, Rolling Hills Research Corporation, Nov. 2013.
22. Lakshminarayana, B., "*Turbulence Modeling for Complex Shear Flows*," *AIAA Journal*, Vol. 24, No. 12, 1986, pp. 1900-1917.
23. Lee, B.J. and Kim, C., "*Automated Design Methodology of Turbulent Internal Flow Using Discrete Adjoint Formulation*," Aerospace Science and Technology, Vol. 11, Nos. 2 and 3, 2007, pp. 163-173.
24. Mattingly, J. D., *Elements of Propulsion: Gas Turbines and Rocket.* AIAA Educational Series: Blacksburg, VA © 2006.
25. McDaniel, D.R. and Morton, S.A., "*Efficient Mesh Deformation for Computational Stability and Control Analyses on Unstructured Viscous Meshes*," AIAA Paper 2009-1363, Jan. 2009.
26. Moore, M., Clarke, S., Stoll, A., Clark, A., MacAfee, S., Foster, T., "*Affordable Flight Testing of LEAPTech*," NASA Aeronautics Research Institute, NASA Aeronautics Research Mission Directorate (ARMD), January 13-15, 2015.
27. Moore, M.D., and Fredericks, W., "*Distributed Electric Propulsion Goals, Approaches, Concepts, Benefits, and Tools*," NASA Langley, © 2012.
28. Moore M., Goodrich K., Viken J., Smith J., Fredericks B., Trani T., Barraclough J., German B., Patterson M., "*High-Speed Mobility through On-Demand Aviation*," AIAA 2013-4373, Aviation Technology, Integration, and Operations Conference, Los Angeles, CA, August 2013.
29. Nicholai, L. M. and Carichner, G. E., *Fundamentals of Aircraft and Airship Design.*
30. AIAA Educational Series: AIAA, Reston, VA, 2010.
31. Oberkampf, W. L., Roy, C. J., *Verification and Validation in Scientific Computing.* Cambridge University Press : Cambridge, UK, Copyright 2010.
32. Roache, P. J., *Fundamentals of Verification and Validation.* Hermosa Publishers: Socorro, New Mexico, Copyright 1999, 2009.
33. Roskam, J. and Fillman, Greg. *Design for minimum fuselage drag.* 0021-8669 vol.13 no.8 (639-640): Journal of Aircraft, 1976.

34. Schiltgen, B. T., Gibson A. R., Keith J. D., *Mission Performance Comparisons of Subsonic Airliners with Current and Future Propulsion Technologies,* AIAA-2010-279-576 : 48th AIAA Aerospace Sciences Meeting Including the New Horizons Forum and Aerospace Exposition, Orlando, FL, 2010
35. Smith, C.F., Bruns, J.E., Harloff, G.J., and DeBonis, J.R., "*Three-Dimensional Compressible Turbulent Computations for a Diffusing S-Duct"*, NASA CR 4392, 1991.
36. Smith, N. F., *High-Speed Investigation of Low-Drag Wing Inlets,* NACA WARTIME REPORT, Advanced Confidential Report L4I18, Langley Field, VA, September, 1944.
37. Stoll, A.M., Bevirt, J., Moore, M.D., Fredericks, W.J., Borer, N.K., "*Drag Reduction Through Distributed Electric Propulsion*," Aviation Technology, Integration, and Operations Conference, AIAA, June 2014.
38. Strang, W.Z., Tomaro, R.F, and Grismer, M.J., "*The Defining Methods of Cobalt$_{60}$: A Parallel, Implicit, Unstructured Euler/Navier-Stokes Flow Solver*," AIAA Paper 99-0786 Jan. 1999.
39. Taskinoglu, E. and Knight, D., "*Multi-Objective Shape Optimization Study for a Subsonic Submerged Inlet*," Journal of Propulsion and Power, Vol. 20, No. 4, 2004, pp. 620-633.
40. Tecnam, "*P2006T Aircraft: Report No. 2006/001, Main Features & Description*," 6th Edition, Revision 1, May 2009.
41. Tomaro, R.F., Strang, W.Z., and Sankar, L.N., "*An Implicit Algorithm for Solving Time Dependent Flows on Unstructured Grids*," AIAA Paper 97-0333, Jan. 1997.
42. von Doenhoff, A.E., and Horton, E.A., "*Preliminary Investigation in the NACA Low-Turbulence Tunnel of Low-Drag Airfoil Selections Suitable for Admitting Air at the Leading Edge*." Advanced Confidential Report, National Advisory Committee for Aeronautics (NACA), Originally Issued July 1942.
43. Welborn, S.R., Reichert, B.A., and Okiishi, T.H., "*Experimental Investigation of the Flow in a Diffusing S-Duct*," AIAA Paper 92-3622, 1992.
44. Zhang, W., Knight, D., and Smith, D., "*Automated Design of a Subsonic Diffuser*," Journal of Propulsion and Power, Vol. 16, No. 6, pp. 1132-1140, 2000.